Lappeenranta University of Technology
School of Energy Systems
Master`s Degree Programme in Electrical Engineering

Pavel Mirlenko

Direct force control of AMB-rotor system

Examiner: Professor Olli Pyrhönen

Supervisor: Researcher, D.Sc. Rafal Jastrzebski

ABSTRACT

Lappeenranta University of Technology
School of Energy Systems
Master`s Degree Programme in Electrical Engineering

Pavel Mirlenko

Direct force control of AMB-rotor system

Master's Thesis

2017

64 pages, 37 figures, 11 tables

Examiner: Professor Olli Pyrhönen

Keywords: AMB, control, force control, DFC

Active magnetic bearing (AMB) is a bearing type that supports a rotor with a magnetic force without any physical contact. AMBs require continuous control as an AMB-rotor system is unstable. Various control principles could be used in the AMB-rotor system: feedback control, cascaded control with different inner control loops, and model-based control. In control of electrical motors, the DTC principle and the flux estimation provide very fast control responses by power switches direct control. In AMB control systems the corresponding principle can be adapted for direct control of forces without a need for cascaded control loops. In this thesis, the feedback control and the cascaded control are studied, the direct force control (DFC) principle is designed. The rotor is considered to be rigid and the 2 degree of freedom AMB is studied. The comparison of the control principles responses is analyzed. The designed DFC principle provides better dynamics than the conventional control principles.

ACKNOWLEDGEMENTS

This thesis was carried out at School of Energy Systems, Lappeenranta University of Technology.

I wish to thank the International Department of the Saint Petersburg Electrotechnical university "LETI" for the ability to study on the Double Degree Programme at Lappeenranta University of Technology.

I would like to express my gratitude to my supervisor D.Sc. Rafal Jastrzebski for his scientific guidance and support. I wish to thank the Professor Olli Pyrhönen for the guidance and productive discussions.

Special thanks to D.Sc. Victor Vtorov for his invaluable help with the studying process throughout the academic year.

Special thanks to my brother Aleksandr Mirlenko for his encouragement, support and reasonable comments and advices.

Last but not least many thanks to my parents for their love.

Pavel Mirlenko

Lappeenranta University of Technology

August 31, 2017

TABLE OF CONTENTS

1. INTRODUCTION 10

1.1 Characteristics of active magnetic bearings 10

1.2 AMB system structure 11

1.3 Radial force generation.....13

1.4 Electromagnets 14

1.5 Rotor dynamics.....19

1.6 Actuator dynamic approximation 21

1.7 Summary.....24

2. MODELLING.....25

2.1 Magnetic actuator 25

2.2 Differential driving mode 29

2.3 Disturbance and reference signal.....30

2.4 Values for the simulation.....31

2.5 Summary.....31

3. MAGNETIC BEARING CONTROL.....32

3.1 General control structure 32

3.2 PID controller design.....33

3.3 Inner current control.....34

3.4 Inner voltage control.....38

3.5 Inner flux control.....39

3.6 Control methods comparison.....40

3.7 Nonlinear control principles comparison 43

3.8 Summary.....45

4. DIRECT FORCE CONTROL 46

4.1 Direct torque control.....46

4.2 Mathematical model 47
4.3 Control principle 49
4.4 Simulation results 53
4.5 Comparison with other control principles 57
4.6 Summary 59
CONCLUSION 61
REFERENCES 63

NOMENCLATURE

Symbols

a	acceleration
B	magnetic flux density
d_A	radial bearing A location with respect to the gravity center
D	damping matrix
$\boldsymbol{D_e}$	electric flux density
F_m	attractive magnetic force
F	force matrix
G	gyroscopic matrix
H	magnetic field strength
I_y	transversal moment of inertia along the y axis
i	current
$\boldsymbol{J}$	current density
K	stiffness matrix
k_i	current stiffness
k_u	motion induced voltage coefficient
k_x	position stiffness coefficient
L	inductance
l_0	nominal air-gap
l_{air}	airgap
l_{flux}	flux length in an electromagnet
m	mass
M	mass matrix
N	number of coil turns
Q	displacement vector
R	resistance
s	Laplace variable
S_{air}	the smallest cross section area of an electromagnet
$\boldsymbol{T}$	transformation matrix

t	time
U	voltage
w_{bw}	power bandwidth
W_{ce}	co-energy
W_{fe}	stored magnetic energy
x	rotor displacement
μ_0	permeability of vacuum
τ_{cl}	closed-loop time constant
Φ	magnetic flux
χ	force acting angle
ψ	magnetic flux linkage
$\mathbf{\Omega}$	rotational speed
ω	angular frequency
$\nabla\times$	curl operator

Subscripts

A	*A* end of the rotor with bearing *A*
air	air
B	*B* end of the rotor with bearing *B*
bias	bias
bw	bandwidth
c	control
cl	closed loop
DC	direct current
del	delay
dyn	dynamic
ff	feed-forward
in	input
m	measured
max	maximal
out	output

p	proportional
ref	reference
rise	settling
sys	system
tri	triangular
x	*x* axis

LIST OF ABBREVIATIONS AND SYMBOLS

AMB	active magnetic bearing
DFC	direct force control
DOF	degree of freedom
DTC	direct torque control
FOC	field-oriented control
IGBT	insulated-gate bipolar transistor
LQG	linear quadratic Gaussian
Maglev	magnetic levitation
PID	proportional–integral–derivative Controller
PM	permanent magnet
PWM	pulse width modulation

1. INTRODUCTION

The idea of body levitation in the air has been a dream of humankind since the ancient times. Not far from nowadays the magnetic levitation phenomenon was discovered, and in the 20th century the magnetic suspension principle was for the first time applied in the bearings. Since that time the magnetic suspension of rotors in electrical machines has considerably evolved. The main reasons for the advances in technology are the significant progress in power electronics components and information processing, as well as theoretical development of control systems design.

The thesis objective is to design the direct force control (DFC) principle, that is based on the direct torque control (DTC) used in electrical drives. During the research two loops control systems are studied and later compared with the invented DFC principle. The control principles are modelled and then simulated in the MATLAB Simulink software.

The first chapter contains the background information about the AMB and the equations describing the processes in the AMB-rotor system. The second chapter comprises the system modelling processes and the values required for the simulations. In the third chapter the conventional magnetic bearing control principles are presented. In the fourth chapter the DFC principle is presented and discussed.

1.1 Characteristics of active magnetic bearings

In an active magnetic bearing (AMB) magnetic force allows to support a rotor in an electrical machine without any physical contact. This feature allows to eliminate the important issue of drive maintenance – bearing lubrication and renewal [1]. Due to the absence of lubrication oil motor drives designed on the magnetic levitation principle can be used in applications where conventional bearings cannot provide the desired features. Among the other important benefits of AMBs the following can be stated:

- High rotational rotor speed, that is limited only by the rotor material strength.
- Active rotordynamics control through the bearings [2].
- AMBs ensure high vibration insulation and lower power losses in comparison with the fluid film bearings [3].

In accordance with the mentioned benefits the list of possible applications is as follows:

- medical and pharmacy equipment;
- outer space equipment;
- equipment exploited in severe environments and undergoing radiation and poisonous substances;
- electrical drives operating in vacuum without contamination;
- MAGLEV trains;
- precise machine tools [4].

However, several drawbacks are mentioned in [3-5] and [6].

- Load capacity failure due to a breakdown of any single component.
- Maintenance operations are impossible without qualified personnel.
- In general, higher costs, weight and space requirements in comparison with conventional bearings.

1.2 AMB system structure

AMB is a clear example of a mechatronic product, as the hardware part of a system with AMBs comprises mechanical components aggregated with electronic elements and information processing unit. Software of an AMB system is another crucial part, and the designed control models define the further system efficiency. In a typical mechatronic system forces and motions are produced in accordance with the input signals processed by the system.

AMB system consists of three main parts: AMBs, a control unit and auxiliary bearings. Generally, in 5-DOF system the rotor is levitated by two radial bearings and one axial bearing. Radial bearings provide the generation of magnetic forces in two dimensions along x and y axes; axial bearing generates force along z axis. Auxiliary bearings are used to prevent a rotor touchdown under the condition of high shock load or other failures in the bearing winding or other circuitry. The electromagnetic levitation principle for the 5-DOF magnetic bearing system is shown in Figure 1.1.

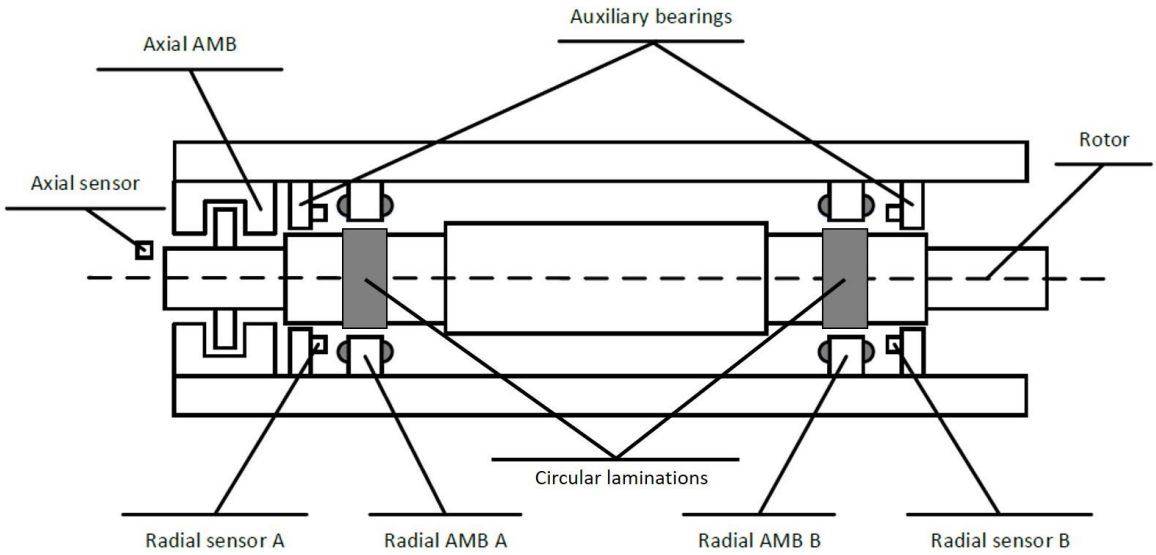

Figure 1.1 Principle of electromagnetic levitation for 5-DOF magnetic bearing system.

In AMB-rotor system a rotor is a complicated device consisting of several components. A rotor is a solid steel shaft with a stack of circular laminations fitted to the shaft at the area of radial AMBs installation. The laminations are used to prevent high eddy current losses and to ensure high magnetic permeability. A rotor also includes a solid steel disk used for the axial AMB. The axial AMB stator is used for a double-acting thrust bearing installation [4]. The operating position range, that is lately referred to as $(x_{min,}x_{max})$ and (y_{min},y_{max}), is determined by the airgap length between the auxiliary bearings and the rotor.

The rotor position should be kept in the operating position range. For the rotor displacement evaluation purpose position sensors are used. Among the specific requirements to the position sensors are the following features: the sensors should be contactless, have decent linearity and sensitivity in the measurement range, as well as low noise susceptibility. In accordance with the research of Boehm et al. [7], the eddy current transducer is the most suitable sensor type for accurate measurements in small operating range. The eddy current transducer fulfills the mentioned requirements, though the price is considerably high. The typical eddy current transducer structure is illustrated in Figure 1.2.

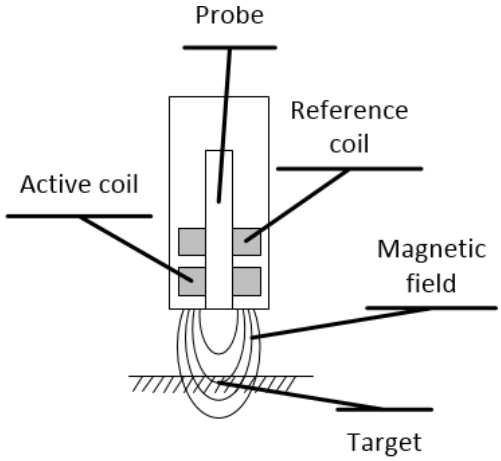

Figure 1.2 Eddy current transducer structure.

In the sensor probe the magnetic field of high frequency is induced by the alternating currents inside the active coil. Faraday's law stands that the magnetic flux density changes on the conducting object surface induce the rotating electric field. Eddy currents are generated by the rotating electric field and, thus, the energy is dissipated due to the magnetic flux density reduction. The amount of energy dissipated and both the oscillating current amplitude and phase are dependent on the clearance between the probe and the target. The oscillating current is processed, and the corresponding voltage signal is outputted. The reference coil is used to compensate the changes in temperature and to balance the output signal.

1.3 Radial force generation

The rotor radial force generation principle in AMB is illustrated in Figure 1.3. Stator core surrounds a rotating shaft. Strong magnetic attractive forces are generated by eight magnetic poles in N,S,N,S sequence between the rotor and stator cores as illustrated.

In the Figure 1.3(a) a vector sum of the radial forces generated by the magnetic poles equals zero, as the flux densities are equal. However, in Figure 1.3(b) the right electromagnet has stronger flux density than the remaining ones, what results in the rotor radial force generation in the direction represented by the black arrow.

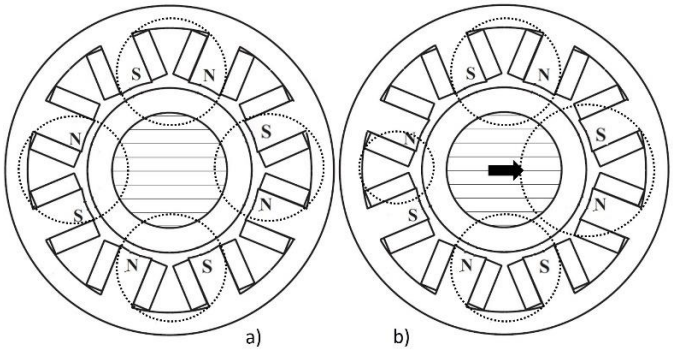

Figure 1.3 Radial force generation by: a) balanced airgap flux density; b) unbalanced airgap flux density. Adapted from [4].

1.4 Electromagnets

The simple structure of 1-DOF magnetic levitation system is presented in Figure 1.4. The radial displacement along x-axis is detected by the displacement sensor. The controller is fed with the feedback signal coming from the sensor, and provides the control to the current regulator. The control law determines the levitation stability and both stiffness and damping of a magnetic suspension. A series-wound coil around the electromagnet is excited by the reference control currents outputted from the current regulator. By controlling the currents in the coil, the electromagnetic flux ψ is changed, what results in the magnetic attractive forces change. The flux path is represented by dashed line. It is clear, that the airgap is crossed by the flux twice along x-axis.

To provide the object levitation the generated upward magnetic attractive force must be sufficient to counteract the gravity. Thus, the generated attractive force should be opposite in direction to the gravity force:

$$F_m = -F_g = -(m * g) = m * g, \tag{1.1}$$

where F_m, F_g, g – attractive magnetic force, gravity force and gravity acceleration, respectively.

The radial force F_x is described as follows:

$$F_x = K_i i_c + K_x x, \tag{1.2}$$

where K_i is an actuator gain (current stiffness), K_x – position stiffness, i_c – reference control current, x - radial displacement along x-axis.

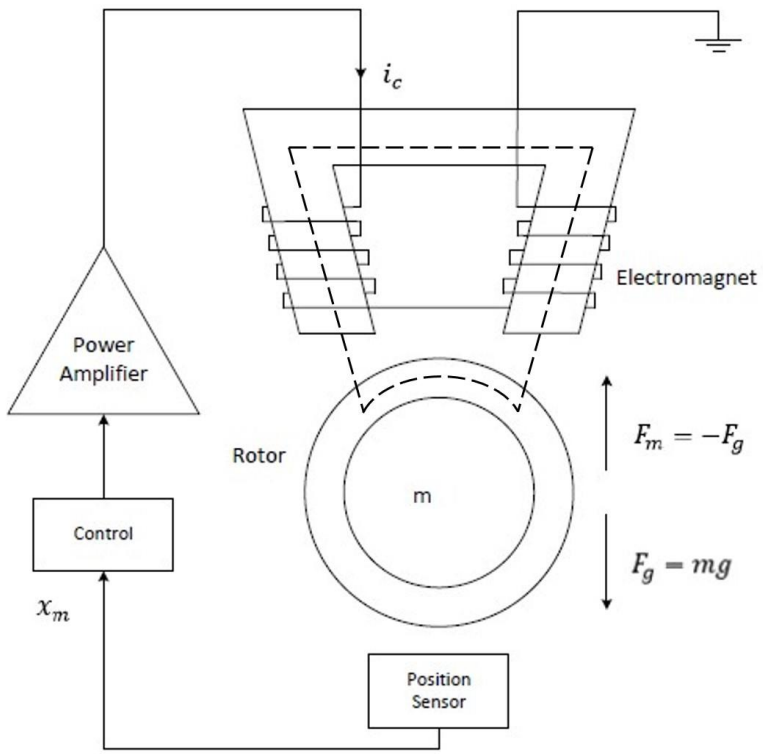

Figure 1.4 Magnetic levitation system.

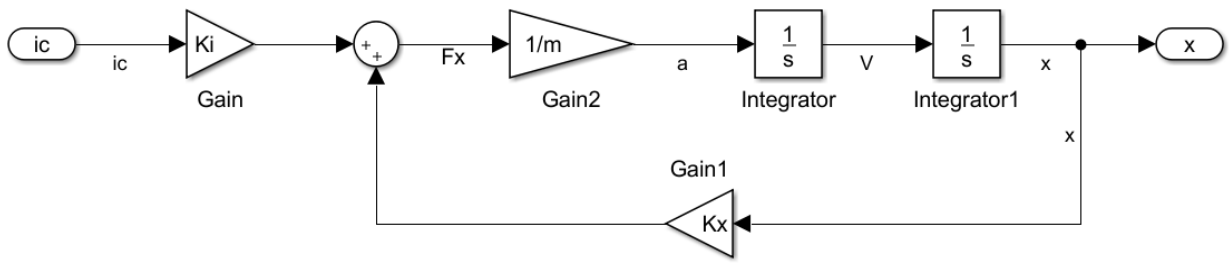

Figure 1.5 Simple block diagram of magnetic levitation system.

Illustrated in Figure 1.5 block diagram represents equation 1.2, in which the output variable is the radial displacement along the x-axis. Block diagram for the operation in the y-axis direction can be obtained in analogy. The radial displacement x is obtained as a double integration of acceleration a with the use of Laplace operators $1/s$. It is clear from the block diagram, that K_x is a gain in the positive feedback loop, thus the presented system is unstable. In accordance with the block diagram, the system transfer function is derived in equation 1.3.

$$G(s) = \frac{K_i}{ms^2 - K_x} \tag{1.3}$$

Transfer function poles:

$$s = \pm\sqrt{\frac{K_x}{m}} \tag{1.4}$$

One of the poles is placed in the right half plane, thus a negative feedback controller is necessary for stable operation.

Coefficients K_x and K_i for the system linearized about the operating point are defined as follows [4]:

$$K_x = \frac{\mu_0 N^2 S_{air} i_{bias}^2 cos\chi}{l_0^3} \tag{1.5}$$

$$K_i = \frac{\mu_0 N^2 S_{air} i_{bias} cos\chi}{l_0^2} \tag{1.6}$$

where μ_0 – vacuum permeability, N – number of coil turns, S_{air} – the smallest cross-section area of the electromagnet, i_{bias} – biasing current, χ – force acting angle $\left({}^{\pi}/_{8}\right)$.

An electrical equivalent circuit for the magnetic circuit of the electromagnet is presented in Figure 1.6.

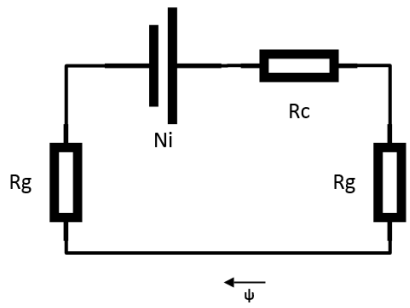

Figure 1.6 Equivalent magnetic circuit.

The voltage source Ni represents the MMF generated by the current in the winding. R_g and R_c represent the magnetic resistance in the airgap and in the electromagnet, respectively. Magnetic resistances are calculated as follows:

$$R_g = \frac{l_{air}}{\mu_0 wl}$$

$$R_c = \frac{l_{flux}}{\mu_0 \mu_r wl} \tag{1.8}$$

The flux ψ could be calculated as follows:

$$\psi = \frac{Ni}{2R_g} = \frac{Ni\mu_0 wl}{2l_{air}} \tag{1.9}$$

From the flux equation, the flux density B in the airgap could be expressed:

$$B = \frac{\psi}{wl} = \frac{Ni\mu_0}{2l_{air}} \tag{1.10}$$

Based on the flux density in the airgap B, the field energy stored in the air-gap could be expressed. Co-energy W_{ce} and a stored magnetic energy W_{fe} could be considered equal, assuming magnetic circuit being linear. For the electromagnet illustrated in Figure 1.4 the magnetic co-energy stored in the air-gap is expressed as follows:

$$W_{ce} = \int_V \int_0^H BdHdV = \int_V \int_0^H HdBdV = \frac{1}{2\mu_0} \int_V B^2 dV = \frac{1}{2\mu_0} B^2 S_{air} 2l_{air} \tag{1.11}$$

In accordance with the virtual work principle, the force in the electromagnet could be defined as a magnetic co-energy W_{ce} derivative with respect to the displacement x [4].

$$f = \frac{\partial W_{ce}}{\partial x} = \frac{B^2 S_{air} cos\chi}{\mu_0} \tag{1.12}$$

The attractive force generated by the electromagnet can be obtained from the equation as follows:

$$f = \frac{\mu_0 N^2 i^2 S_{air} cos\chi}{4l_{air}^2} \tag{1.13}$$

The total force for two electromagnets acting along one axis can be expressed as a difference of forces produced by the electromagnets:

$$f = f_{x,1} - f_{x,2} = \frac{\mu_0 N^2 S_{air} cos\chi}{4}\left(\frac{i_{x,1}^2}{(l_0 - x)^2} - \frac{i_{x,2}^2}{(l_0 + x)^2}\right) \tag{1.14}$$

For the convenience's sake, the coil currents $i_{x,1}$ and $i_{x,2}$ should be limited and the bias current should be added. Equation 1.14 could be linearized with the bias i_{bias} current:

$$\begin{gathered} i_{x,1} = \max(i_{bias} + i_c, 0) \\ i_{x,2} = \max(i_{bias} - i_c, 0) \\ f_x = \frac{\mu_0 N^2 S_{air} cos\chi}{4}\left(\frac{(i_{bias} + i_c)^2}{(l_0 - x)^2} - \frac{(i_{bias} - i_c)^2}{(l_0 + x)^2}\right) \end{gathered} \tag{1.15}$$

Current stiffness k_i and position stiffness k_x could be obtained by taking the derivatives from the force equation:

$$k_i = \frac{\partial f}{\partial i_c} = \frac{0.000023544\, x^2 + 5.886e - 9xi_c + 2.3544e - 11}{-0.000002\, x^2 + x^4 + 1.0e - 12} \tag{1.16}$$

$$k_x = \frac{\partial f}{\partial x} = \frac{2.943 * 10^{-9} {i_c}^2 + 4.7088 * 10^{-5} xi_c + 1.88352 * 10^{-7}}{-0.000002\, x^2 + x^4 + 10^{-12}} - \tag{1.17}$$

$$-\frac{(4x^3 - 0.4 * 10^{-5} x)(1.88 * 10^7 x + 2.3544 * 10^{-11} i_c + 0.000023544 x^2 i_c + 2.943 * 10^{-9} x {i_c}^2)}{(-0.000002\, x^2 + x^4 + 10^{-12})^2}$$

Assuming the radial displacement and control current being equal zero, the values of the coefficients could be calculated as follows:

$$k_i = 23.544 \tag{1.18}$$

$$k_x = 1.884 \cdot 10^5 \tag{1.19}$$

Later on, equation 1.13 is used as a nonlinear plant model. The total force produced by two electromagnets acting along the same axis is calculated as a difference of each electromagnet force. The linear plant model described by equation 1.2 is used for the preliminary studies.

1.5 Rotor dynamics

Two types of rotor are considered in this thesis: a rigid rotor and a flexible rotor. The rigid rotor is characterized by flexible eigenfrequencies above the displacement controller bandwidth and the maximum rotational speed. The flexible rotor keeps flexible eigenfrequencies at low frequencies, that could be changed by the displacement controller. For a flexible rotor, the elastic dynamics modelling is required [6, 8].

In the controller design process the rotor is considered to be a rigid body, i.e. the rotor is modelled as two point masses, that are located in the radial bearings installation place. Considering that the rotor has constant mass, and the transfer function introduced in equation 1.3 is linear, the force acting along the x-axis could be expressed:

$$F_x = ma = m\ddot{x} = K_i i_c + K_x x \tag{1.20}$$

For the rotor radial suspension along the x- and y-axis, four independent equations (1.20) constitutes the rotor model. However, the transversal motion and tilting motion are not considered by four independent equations. For the mentioned motions consideration, 2-DOF system is studied, that is a rotor with neglected coupling between two coordinate planes (x,z), (y,z) and neglected rotor rotation.

In accordance with the Newton's II law, the linearized motion equation for the rigid and flexible modes is expressed as follows:

$$\boldsymbol{M}\ddot{\boldsymbol{q}}(t) + (\boldsymbol{D} + \boldsymbol{\Omega}\boldsymbol{G})\dot{q}(t) + \boldsymbol{K}\boldsymbol{q}(t) = \boldsymbol{F}(t) \tag{1.21}$$

where **M** – mass matrix, **q** – displacement vector, **D** – damping matrix, **Ω** – rotational speed, **G** – gyroscopic matrix, **K** – stiffness matrix, and **F** – force.

However, some system's components like bearings, seals and dampers could not be linearized due to its strong nonlinear behavior [9]. Indeed, for linearized equation 1.21 application, several requirements should be fulfilled:

- the displacements from the reference points are neglectable in comparison with the rotor dimensions;
- axisymmetric rotor behavior;

- constant rotational speed.

Under the assumption that the rotor is a rigid body, the damping matrix $\boldsymbol{D}$ equals zero. If the rotor is studied in a single plane only, the gyroscopic matrix $\boldsymbol{G}$ is considered to be zero as well [9]. Taking into account the mentioned assumptions, the 2-DOF rigid rotor motion equation could be expressed based on equations 1.2 and 1.21.

$$\boldsymbol{M}_g\ddot{\boldsymbol{x}}_g = \boldsymbol{T}_1\boldsymbol{K}_x\boldsymbol{x}_b + \boldsymbol{T}_1\boldsymbol{K}_i\boldsymbol{i}_c = \boldsymbol{F}_g \tag{1.22}$$

$$M = \begin{bmatrix} m & 0 \\ 0 & I_y \end{bmatrix};\ K_x = \begin{bmatrix} k_x & 0 \\ 0 & k_x \end{bmatrix}; K_i = \begin{bmatrix} k_i & 0 \\ 0 & k_i \end{bmatrix};\ i_c = \begin{bmatrix} i_{c,A,x} \\ i_{c,B,x} \end{bmatrix}, \tag{1.23}$$

where I_y – transversal moment of inertia along the y axis. Subscripts A and B in the control current indicates the bearings A and B, respectively, that are illustrated in Figure 1.7. By the vector $\boldsymbol{x} = [x \quad \beta_y]^{\mathrm{T}}$, the transversal and tilting motions are considered. The displacement vector $\boldsymbol{x}_b = [x_A \quad x_B]^{\mathrm{T}}$ comprises the rotor displacements for bearings A and B. Subscripts g and b indicates the coordinate frames of the gravity center and the bearings, respectively.

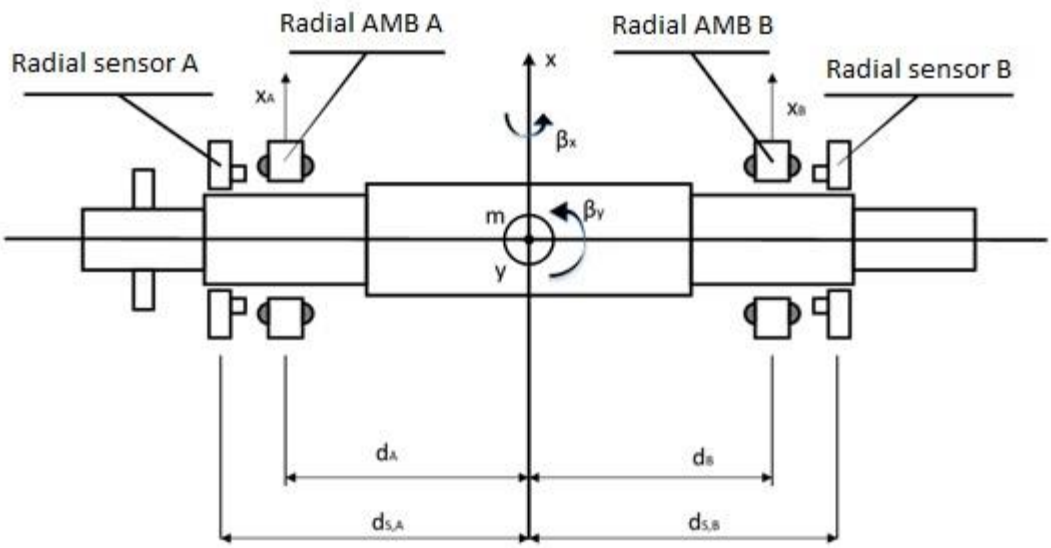

Figure 1.7 Radial rigid rotor model.

For the transformation of forces acting in bearings A and B in the gravity center reference frame, the force components are multiplied by the transformation matrix $\boldsymbol{T}_1$:

$$\boldsymbol{T}_1 = \begin{bmatrix} 1 & 1 \\ -d_A & -d_B \end{bmatrix}, \tag{1.24}$$

where d_A, d_B express the radial bearings location with respect to the gravity center as shown in Figure 1.7.

As a matter of convenience, the motion equation could be transformed to the bearing coordinate frame. The motion equation is expressed as follows:

$$\boldsymbol{M}_b \ddot{\boldsymbol{x}}_b = \boldsymbol{K}_x \boldsymbol{x}_b + \boldsymbol{K}_i \boldsymbol{i}_c = \boldsymbol{F}_b \ , \tag{1.25}$$

where the mass matrix is in the bearing coordinate frame. The relation between the two coordinate frames is defined by the transformation matrices $\boldsymbol{T}_1$ and $\boldsymbol{T}_2$, that are related to the gravity center coordinate frame and bearing coordinates, respectively. The relation between the matrices is expressed as follows:

$$\boldsymbol{T}_2 = \boldsymbol{T}_1^{-T} \tag{1.26}$$

Based on the equations mentioned above, the mass matrix and the displacement vector could be expressed:

$$\boldsymbol{x}_b = \boldsymbol{T}_1^T \boldsymbol{x}_c \tag{1.27}$$

$$\boldsymbol{M}_b = \boldsymbol{T}_2^T \boldsymbol{M}_c \boldsymbol{T}_2 \tag{1.28}$$

In the described model, the rotor dynamics are expressed as two uncoupled 2-DOF equations, one in the (x,z) coordinate plane and the other in the (y,z) plane.

1.6 Actuator dynamic approximation

A typical current controller [2,4,6,10] comprises the proportional gain G_p and feed-forward gain G_{ff}, that usually equals zero. Thus, the current controller can be expressed as

$$u_{ref} = G_{ff} i_{ref} + G_p (i_{ref} - i_m) \tag{1.29}$$

where u_{ref}, i_{ref}, i_m – reference voltage, reference current and measured current, respectively.

Under the assumption that $G_{ff} = 0$, the equation 1.38 could be rewritten as

$$u_{ref} = G_p (i_{ref} - i_m) \tag{1.30}$$

Based on the equations 1.30 and 1.39, the closed-loop dynamics could be defined as

$$G_{cl}(s) = \frac{i_m}{i_{ref}} \approx \frac{G_p}{sL + G_p} = \frac{1}{s\tau_{cl} + 1} \tag{1.31}$$

Time constant of the closed loop can be defined by the expected rise time $\tau_{cl} = t_{rise}/\ln(9)$. More detailed approximation of the system's dynamics comprises the time delay added by PWM and transport delay. The delay could be approximated as a shift in time in Laplace domain with the use of Padé approximation.

The nonlinear system could be approximated to the equation as follows:

$$G_{cl}(s) = \frac{G_p G_{del}(s)}{sL + R + G_p G_{del}(s)} \tag{1.32}$$

In the equation 1.41 $G_{del}(s)$ is the first-order Padé approximation of the delay $\xi = -T_{MD} = -3T_S$; T_{MD} is the average modulation delay. G_p is a proportional controller gain.

$$G_{del}(s) = e^{s\xi} = \frac{1}{1 - s\xi} = \frac{1}{sT_{MD} + 1}, T_{MD} = 3T_S \tag{1.33}$$

The final transfer function of the plant model is represented by equation 1.2, and nonlinear system approximation yields:

$$G_{sys}(s) = \frac{K_i}{ms^2 - K_x} \frac{G_p G_{del}(s)}{sL + R + G_p G_{del}(s)} \tag{1.34}$$

Substituting the values from Table 2.1 (see section 2.4) in equation 1.34, and considering the proportional gain value being $G_p = 5$, the final transfer function could be rewritten as:

$$G_{sys}(s) = \frac{0.03472s + 115.7}{1.305e-9\, s^5 + 9.517e-6s^4 + 0.03351s^3 + 54.19s^2 - 685.2s - 1.111e6} \tag{1.35}$$

The current feedback in the inner current control loop could be expressed as [4,6,10]:

$$G_{cl}(s) \approx \frac{w_{bw}}{s + w_{bw}} \tag{1.36}$$

The power bandwidth w_{bw} is calculated as a function of the rise time in the coil L_{dyn}. The rise time t_{rise} is calculated from zero current value to the maximum current value i_{max}.

$$t_{rise} = \frac{1}{U_{DC}} \int_0^{i_{max}} L_{dyn}\,(i, x_0)\, di \tag{1.37}$$

The power bandwidth is expressed as follows: $w_{bw} = \ln(9)\,/t_{rise}$.
With certain assumptions [4,6,10] the dynamic inductance L_{dyn} could be replaced with the nominal inductance value, what results in the power bandwidth equation being:

$$w_{bw} \approx \frac{\ln(9) U_{DC}}{L i_{max}} \tag{1.38}$$

The power bandwidth is selected $w_{bw} = 3200$ [4]. Thus, the value could be substituted in equation 1.36.
Figure 1.8 illustrates Bode diagrams for the different approximation methods. By letter A the system with the approximation based on the bandwidth (equation 1.36) is represented. B stands for the approximation method presented by equation 1.35, though the delay is neglected. The time delay is taken into account in the system C, the approximation method used is the same as in system B. As could be observed, approximations A and B coincide. The obtained equations are to be used in the controller design process.

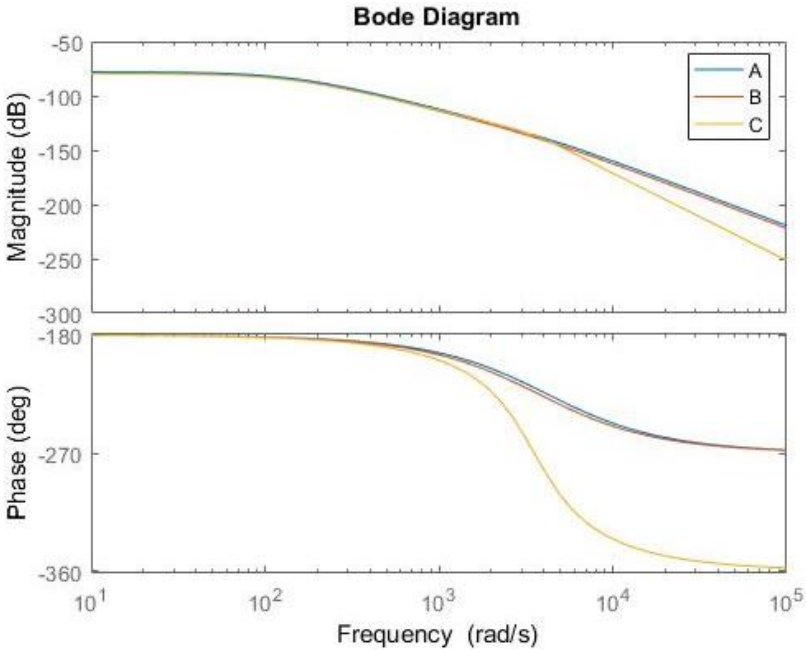

Figure 1.8 Bode diagrams for the different approximation methods.

1.7 Summary

In this chapter, general information required for the magnetic levitation principles understanding was presented. Thus, the typical AMB system structure, magnetic force generation principle and the magnetic levitation system were illustrated. Based on the magnetic levitation system, the system's transfer function was obtained. In addition, the force equations for the electromagnets, and the current stiffness and position stiffness equations were derived. The approximations for the actuator dynamics were presented and the Bode diagram was plotted.

2. MODELLING

In this chapter the major concepts of modelling are presented. The actuator and the rotor block diagrams are illustrated and explained. The nonlinear behavior of the actuator is explained and modelled. In addition, a differential driving mode is presented and discussed. The reference signal, disturbances and initial conditions are mentioned; the parameters values used during the simulations are introduced.

2.1 Magnetic actuator

Figure 2.1 illustrates the current controller structure and the actuator structural components. The reference current i_{ref} is defined as a sum (difference) of control current c, that is the output of the position controller, and the biasing current i_{bias}. The mathematical sign distinguishes the opposite electromagnets acting along the same axis.

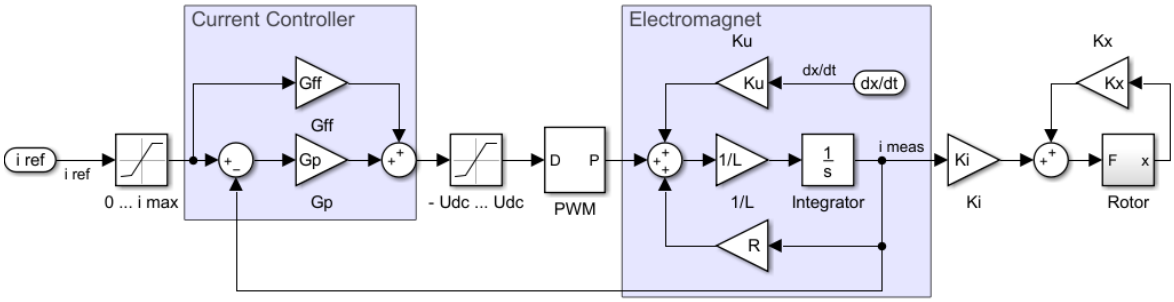

Figure 2.1 Magnetic actuator block diagram.

The coil current is built with the use of the three-phase line-frequency diode rectifier and the power amplifier. The power amplifier used is the H-bridge switching amplifier comprising two diodes and two IGBT switches. The switching pattern is produced with the carrier-based PWM and asymmetric regular sampling [11]. Each IGBT switch has its own control voltage $\pm u_c$, that is compared with the carrier voltage u_{tri}. As a result, the output voltage value changes between zero and $\pm U_{dc}$ (DC link voltage) in accordance with the IGBTs configuration. The mentioned PWM-scheme provides the current harmonics independence from the DC link voltage [11].

In equation 1.2 the linear behavior of actuator subsystem was considered and bearing magnet electrical properties were neglected. However, the coil inductance L, the coil resistance R and the power amplifier voltage should be considered for accurate modelling of system dynamics. The inductance L (also called self-inductance) is dependent on the rotor position x [2]. The dynamic inductance matrix $\boldsymbol{L}_{dyn}$ can be obtained as:

$$\boldsymbol{L}_{dyn} = \frac{d\boldsymbol{\psi}}{di} \tag{2.1}$$

where $\boldsymbol{\psi}$ – coil flux linkage vector. The dynamic inductance matrix $\boldsymbol{L}_{dyn}$ comprises self-inductance and mutual inductance. The total power amplifier voltage represents the sum of the voltage drop, dynamic inductance and motion induced voltage.

$$u = \frac{d\psi}{dt} + Ri = \frac{d\psi}{di}\frac{di}{dt} + \frac{d\psi}{dx}\frac{dx}{dt} + Ri = L_{dyn}\frac{di}{dt} + k_u\frac{dx}{dt} + Ri \tag{2.2}$$

The motion induced voltage coefficient k_u can be approximated as in [4, 10].

$$k_u = i\frac{dL}{dx} \approx 0.5k_i \tag{2.3}$$

Based on equation 2.2 the actuator block diagram is designed as illustrated in Figure 2.1.
For more accurate value, the coefficient could be replaced by the look-up table calculated from the dynamic inductance values. However, analyzing equation 2.2 it could be observed, that the resistance value is of the one ohm order and, thus, the voltage drop term could be neglected in the linear actuator model. However, to make the model more accurate the term should be considered. The motion induced voltage term could be neglected as well [10], though for more accurate modelling, the mentioned terms are considered.
Thus, the inductance nonlinear behavior should be added to the model.
The flux in an electromagnet can be expressed as follows:

$$\Phi = \frac{N i_c \mu_0 w l}{2(l_0 - x)} \tag{2.4}$$

The flux linkage ψ of the coil is calculated as the number of coil turns N times the flux passing through the coil:

$$\psi = \frac{N^2 i \mu_0 w l}{2(l_0 - x)} \tag{2.5}$$

From the flux linkage equation, the inductance L can be calculated as the flux linkage divided by the electromagnet coil current:

$$L = \frac{N^2 \mu_0 w l}{2(l_0 - x)} \tag{2.6}$$

The nominal inductance L_0 under $x = 0$ conditions is defined as follows

$$L_0 = \frac{N^2 \mu_0 w l}{2 l_0} \tag{2.7}$$

Considering that the displacement x is small in comparison with the airgap length, the series expansion can be used

$$\frac{1}{l_0 - x} = \frac{1}{l_0} \frac{1}{(1 - \frac{x}{l_0})} = \frac{1}{l_0}(1 + \frac{x}{l_0} + \left(\frac{x}{l_0}\right)^2 + \left(\frac{x}{l_0}\right)^3 + \cdots) \tag{2.8}$$

Taking into account only the first and the second terms, the inductance is approximated in the following way

$$L = L_0(1 + \frac{x}{l_0}) \tag{2.9}$$

Taking into account equations 1.13, 2.2, 2.3 and 2.9 the electromagnet could be modelled as presented in Figure 2.2.

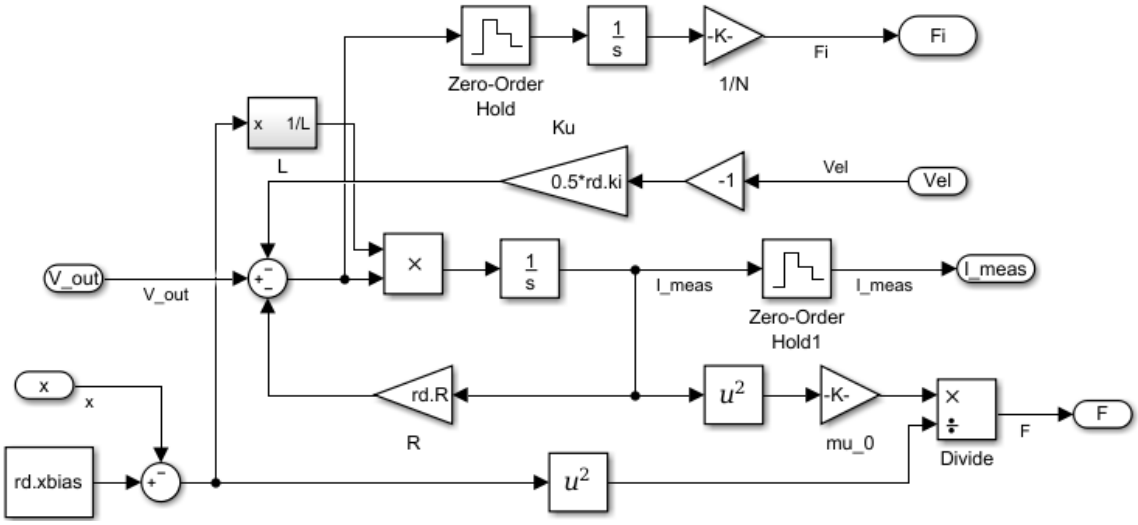

Figure 2.2 Nonlinear electromagnet model.

The presented block diagram allows to consider the nonlinearities in the electromagnet mentioned in section 2.1. The actuator subsystem inputs are the voltage applied to the electromagnet coil, the rotor position and rotational speed.

In the model, it is assumed that the electromagnet coil voltage could be measured. This assumption allows to take into account the motion induced voltage as well as the voltage drop. The measurements are not instant and the Zero-Order Hold blocks are used to model the measurements frequency of 10 kHz. The proportional gain block with the "-1" value before the motion induced voltage coefficient *Ku* block is used to consider the voltage for the opposite electromagnets. In the model the force value of a single electromagnet is calculated, the flux value is obtained, and the coil current is measured. Later on, the presented model is used in all models.

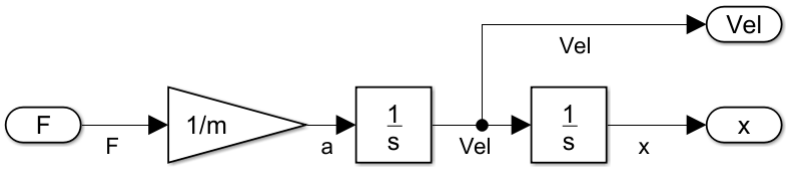

Figure 2.3 Rotor model block diagram.

In Figure 2.3 the rotor model block diagram is presented. In the thesis the rotor is modelled as a two-point mass, and is considered to be a rigid body. The rotor position is obtained by double integration of the acceleration in accordance with equation 1.2. The signal after the first integration represents the rotor rotational speed and is used as the actuator model input signal to calculate the motion-induced voltage.

2.2 Differential driving mode

Presented in Figure 2.1 structure is a 1 DOF system, thus, it is used to describe the rotor control by a single electromagnet. However, in practice two electromagnets act in one direction. To make control more efficient two counteracting electromagnets act, that is called a differential driving mode. The differential driving mode can be explained with the use of Figure 2.4. Two counteracting electromagnets are provided with the coil currents that are obtained as a sum/difference of biasing and control currents. The biasing current is a constant premagnetization current that is used for keeping the object magnetic levitation, while the control current provides the object relocation. With the use of opposite mathematical signs for opposite electromagnets the magnetic force along one axis is controlled by both the increase in magnetic force of one electromagnet and the corresponding decrease in the other's force.

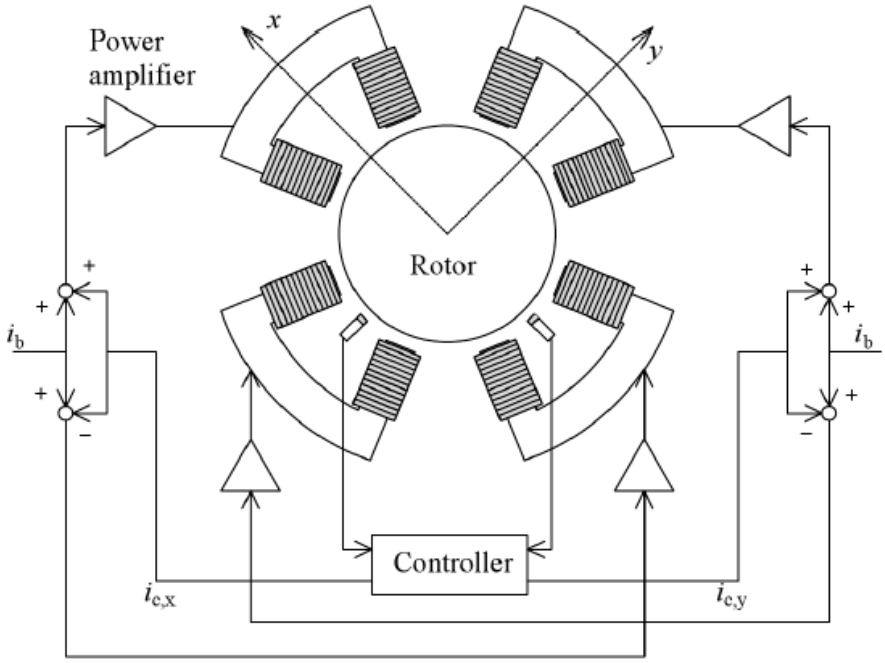

Figure 2.4 Operation principle of a 2 DOF AMB. [8]

Only one coil for each pair of magnetic poles is required for the magnetic bearing structure using differential driving mode. The differential driving mode allows to operate with fewer number of variables. Thus, for a single electromagnet only two control currents could be used instead of four control currents, that are supposed to control separately all four

electromagnets in an AMB. Another option is the differential winding mode principle [12], that is characterized with the bias flux generated with separated coils.

One more option is permanent magnet bearings. In this principle the bias is generated with the use of permanent magnets instead of the coil currents. In comparison with the differential driving mode, the PM biasing results in less variation of force applied to the rotor under the condition of rotor displacement from the operation position [13]. Thus, the system with the PM biasing provides larger load capacity under the rotor displacement conditions. In addition, the overall size of the AMB is smaller [13], and the energy consumption is lower.

2.3 Disturbance and reference signal

In order to examine the system reaction on the disturbances applied, each control method designed later should be tested during simulations. The initial conditions include the initial rotor displacement from the operating point representing the rotor laying on auxiliary bearings. The initial displacement value is equal to $-0.635\ mm$. The system is supposed to bring the response to zero value, what represents the rotor lift-up from auxiliary bearings.

The disturbance could be applied as a force, displacement, control current value, etc. In this thesis, the disturbance applied is the force representing the gravity, thus the force disturbance value is calculated by equation 1.1 and equals $88.824\ N$, considering the rotor mass being $18.127\ kg$ and assuming that the mass acting on one electromagnet (see Figure 1.1) is half of the rotor mass. To simulate the disturbance input in MATLAB Simulink, the step signal block is used.

The reference signal applied is the position reference signal. The signal value is $0.1\ mm$, that is 10% of the operating airgap value. The signal applied allows to test the system's response on the rotor relocation.

In the current thesis, the force disturbance is applied at the time instant of 0.8 seconds and the reference position signal is applied at 1.4 seconds. The force disturbance could be also applied from the operation beginning (0 seconds), though considering the operation of radial bearings acting along the horizontal axis no gravity force value should be considered. Thus, the gravity force impact is added at the time instant of 0.8 seconds to show it separately from the transient response caused by the initial conditions mentioned above.

2.4 Values for the simulation

In this sections the values of the parameters used during the simulations in MATLAB Simulink are presented. The values are selected based on the test rig in the University laboratory and the thesis [4]. All the values used are grouped in Table 2.1.

Table 2.1 Values for the simulation

Parameter	Value
Sample time	100 μs
Rotor mass	18.1273 kg
Number of coil turns	65
Nominal inductance	0.0016 H
Nominal resistance	1.69 Ω
Nominal airgap	0.001 m
Biasing current	8 A
DC link voltage	150 V
Cross section area of an electromagnet	$6 \cdot 10^{-4}$
Position stiffness K_x	$1.8518 \cdot 10^5$
Current stiffness K_i	23.1469

2.5 Summary

In this section, all the necessary information for modeling and simulations was presented. The magnetic actuator was illustrated, and the nonlinear dynamics were taken into account, the rotor model was discussed. The differential driving mode was illustrated and explained to be later used during the controller design process.

In addition, all the values of the parameters used in the models were summarized, and the signals and disturbances, that are used to test the designed controller for its dynamics performance, were presented.

3. MAGNETIC BEARING CONTROL

In this chapter the control principles based on the cascaded control loops are presented. The outer position control remains the same, while the inner control loop varies: the inner current, voltage and flux control loops are studied. In the last section, the comparison of the investigated control methods is presented and discussed, as well as responses on the disturbances and reference signals applied are illustrated.

The major control targets in AMB-rotor system are as follows:

- Elimination of natural instability of the system;
- Provision of the rotor lift-up from the auxiliary bearings at the start of operation;
- Relocation of the rotor along the axis in the operational range in accordance with the refence signal applied without steady-state errors;
- Compensation of actuators nonlinearities;
- Consideration of constant disturbances like the gravity force, measurement noise and mass unbalance.

3.1 General control structure

The general control scheme for a 2 DOF system is assumed to be of a cascaded structure, and consists of two control loops: the first is the inner control loop, the second – the outer position control loop. The general control structure is presented in Figure 3.1.

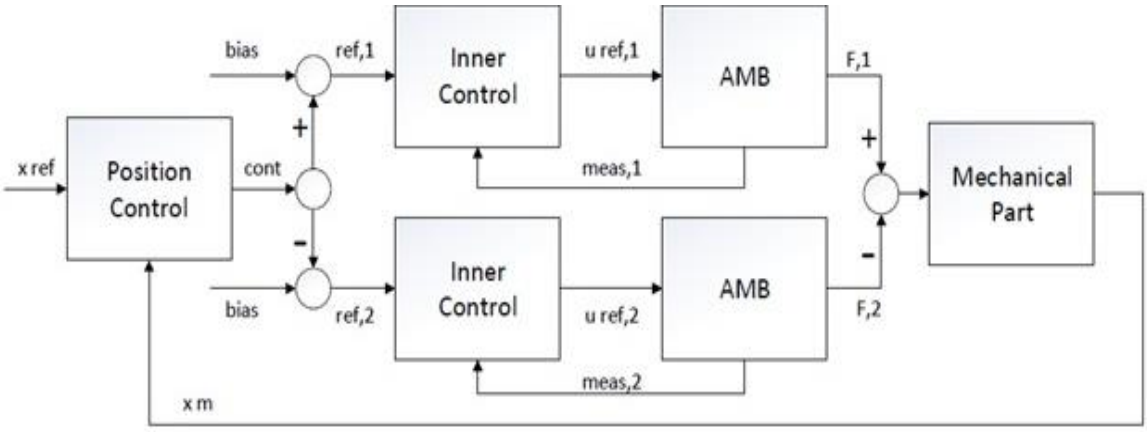

Figure 3.1 General control structure.

The inner control loop is designed to control either current, voltage or flux in actuators. The inner control loop is represented with the measured in electromagnet coils values *meas,1* and *meas,2*. The feedback values are added to the reference values *ref,1* and *ref,2* obtained as a sum/difference of the control value *cont* and the reference value called biasing value *bias*. The rotor displacements from the initial position is controlled by the position control loop represented by xm variable. The inner loop controllers receive the control signals from the position controller. Thus, two opposite electromagnets acting along the same axis are controlled with the single control signal provided by the single position controller. Such a control scheme allows to operate with a fewer number of variables.

Along with current control, voltage control or flux-based control could be designed. In accordance with the studies [2, 6], voltage control provides higher level overall system robustness, though it requires more complicated control schemes. Flux-based control utilizes the flux as a control variable, that is closely related to the generated force. Based on [14], the flux control loop does not lead to the system's instability in contrast with the current control loop. To obtain flux values either Hall sensors or flux estimators could be designed. However, generally, AMBs with an inner current control are used in industry [2].

3.2 PID controller design

Under the assumption that a rotor is rigid, premagnetization current is not reduced in bias linearization, and coupling between channels is relatively small, an AMB-rotor could be viewed as a linear plant [4]. As an outer position controller, a PID controller is used, as it is easy to design, and due to the integral term steady-state errors could be eliminated.

The PID controller working principle is based on the error value $e(t)$ calculation as the difference between a reference signal and a measured output value. A correction is calculated based on the proportional, integral and derivative terms. The PID controller block diagram is presented in Figure 3.2.

The control variable $u(t)$ is used to minimize the error $e(t)$ by adjusting the control variable as a weighted sum:

$$u(t) = K_p e(t) + K_i \int_0^t e(\tau) d\tau + K_d \frac{de(t)}{dt} \tag{3.1}$$

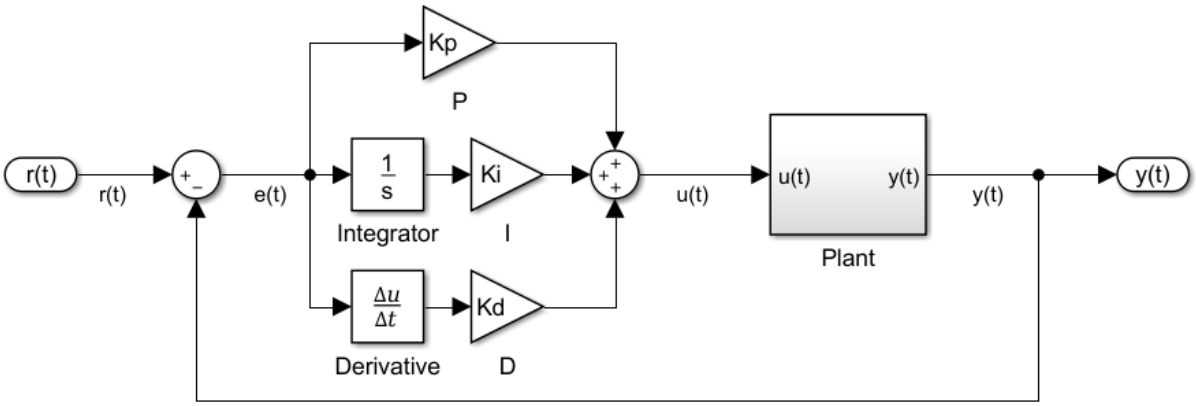

Figure 3.2 PID controller block diagram.

Table 3.1 PID controller parameters

Parameter	Value
Proportional gain K_p	8
Integral gain K_I	40
Derivative gain K_D	0.1

Later on in this chapter, the parameters presented in Table 3.1 are used as the gains in the PID controller. The comparison between the control principles, and between the linear and nonlinear actuator models, are conducted with the same PID controller to make the systems comparable. The use of the same controller for all the control structures investigated is achieved by the use of scaling gains, that have the values of either biasing current or voltage in accordance with the control principle used.

3.3 Inner current control

The general structure of the control system with two loops, that are the inner current control loop and the outer position control loop, is presented in Figure 3.1. In the designed control model the position control is implemented as a PID controller, and the current control comprises proportional and feed-forward gains, the inner current control structure is shown in the Figure 3.3. The model is illustrated in Figure 3.4. The actuator model used in this section is linear and is described by equation 1.2, that is discussed in section 2.1.

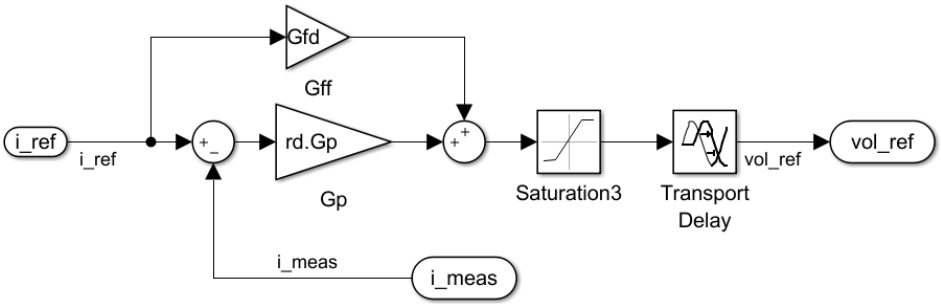

Figure 3.3 Inner current control loop structure.

Current control is based on the measured actuator current feedback mitigating the effect of the coil inductance nonlinear behavior. The feed-forward gain is used for the compensation of the resistive voltage drop effect and steady-state errors elimination caused by PWM [4]. The designed current control can be considered as the first-order process with time delay. Based on D.M. Schneider studies [15], processes with long and varying time are difficult to control and, thus, the inner current control loop should be robust and provide low sensitivity to parameters' variation. During the controller design the fact, that the high proportional gain value adds significant noise to the current output, was taken into consideration.

The Transport Delay block in Figure 3.3 represents the PWM delay [4], [16].

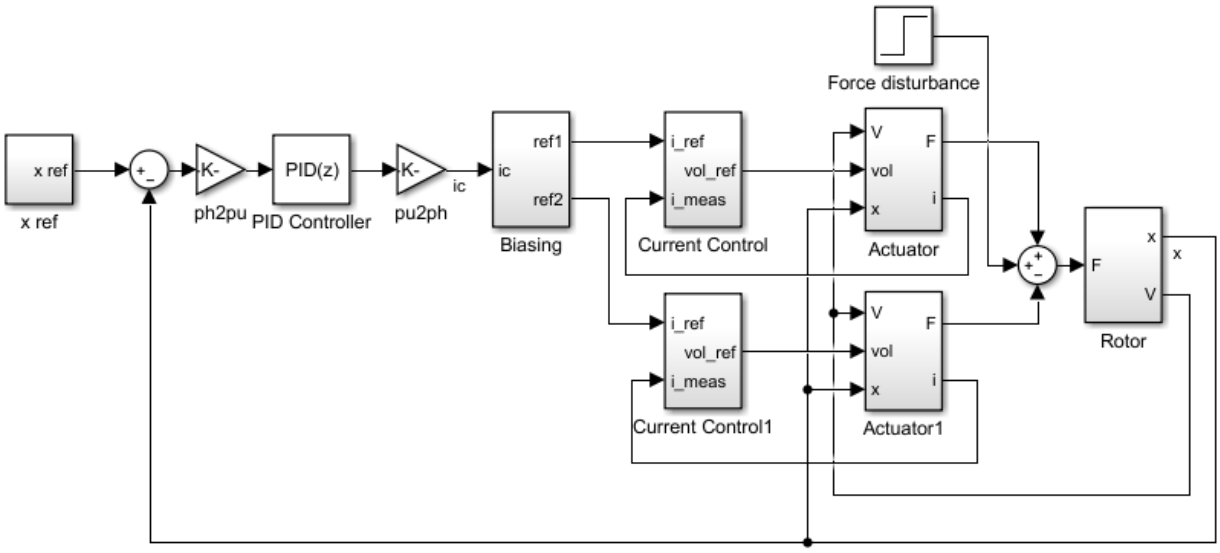

Figure 3.4 Block diagram of the control system with the inner current control loop.

In the model the gains "ph2pu" and "pu2ph" stand for conversion to per-unit values and vice versa, respectively, and represent the system's scaling. The scaling is useful in the models, in which the reference value can be changed, and, thus, the controller tuning should be considered. However, with the use of scaling there is no need for tuning. For the current

control the gain “pu2ph” has the biasing current value. The scaling gain for the voltage and flux control has the biasing voltage value.

In the model the “Actuator” and “Actuator1” subsystems represent two electromagnets acting along one axis. The “Biasing” subsystem represents the reference current calculation for each electromagnet. The reference currents are defined by the biasing current, and the control current, that is the same for both electromagnets. The reference current calculation is the sum of the control and bias currents for one electromagnet, and the substitution for the other, in order to provide an increase in the attractive force of one electromagnet and a decrease in the other’s.

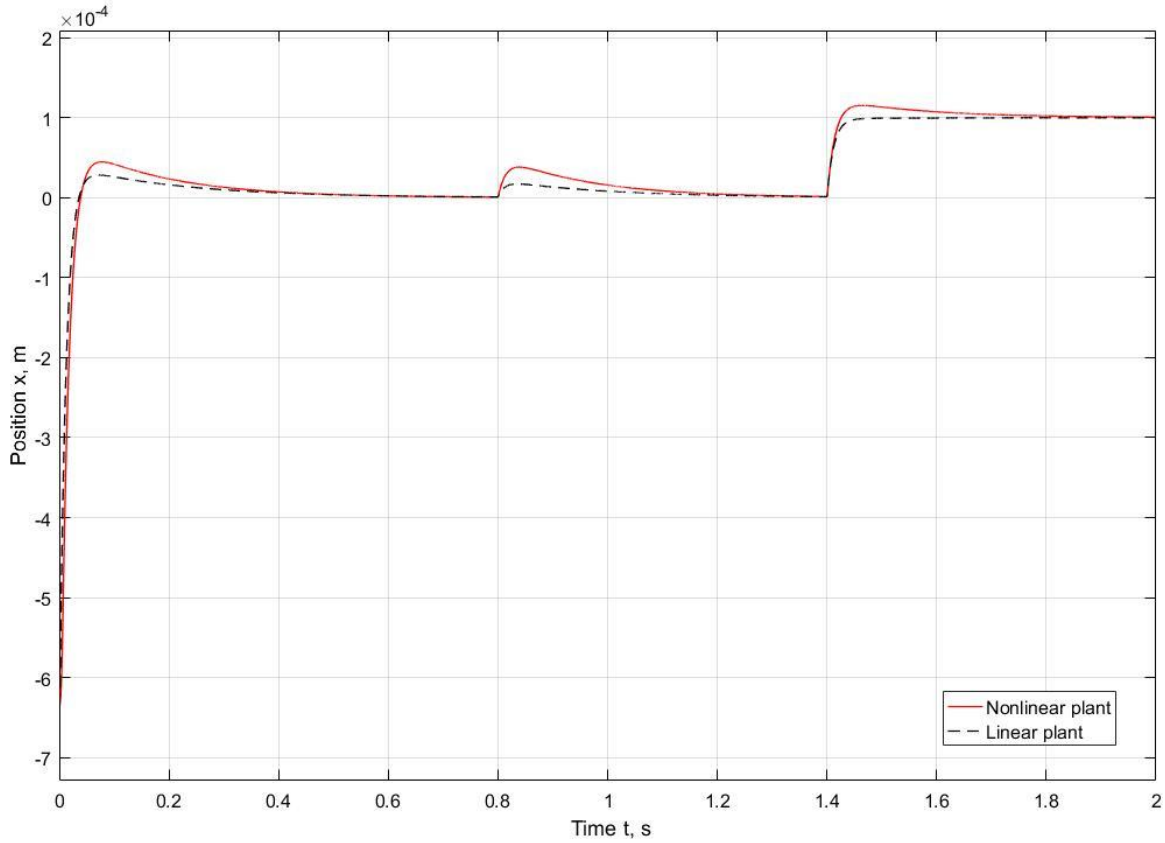

Figure 3.5 Linear plant model response vs nonlinear plant model response of the current controlled cascaded controller structure.

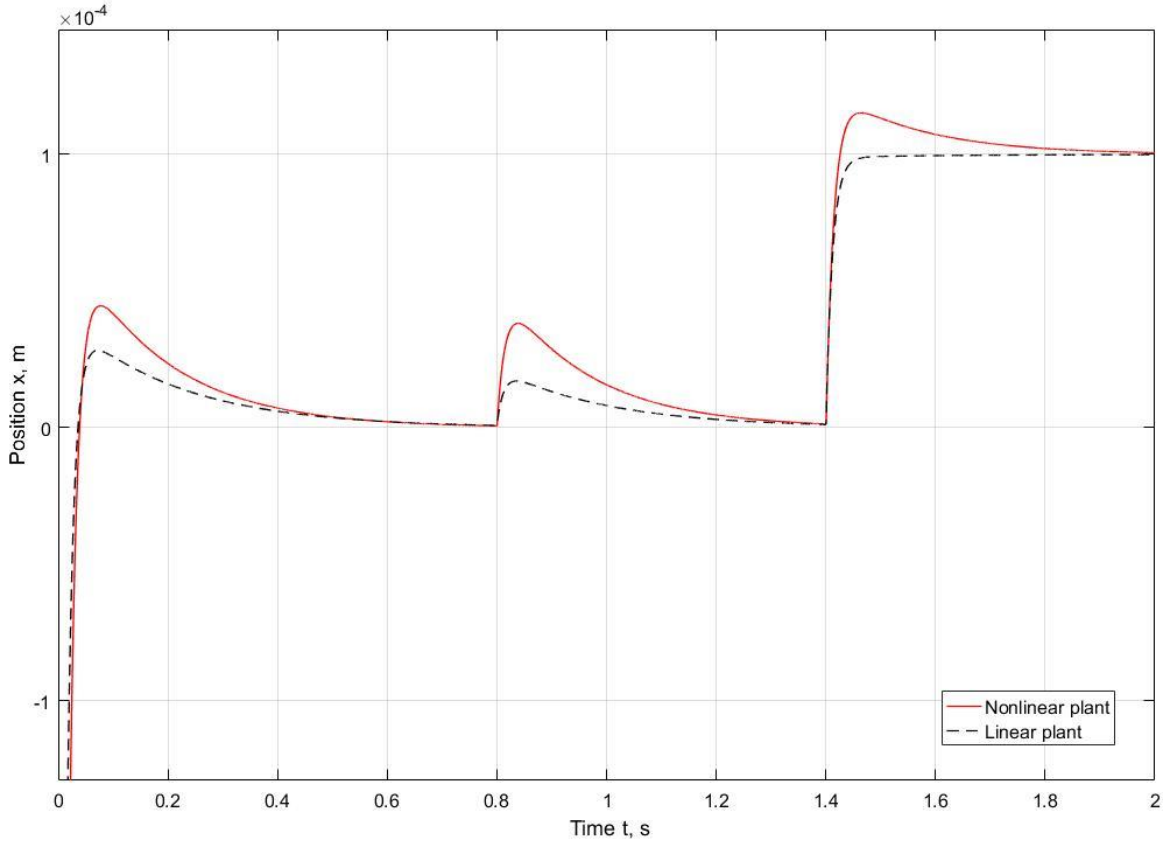

Figure 3.6 Linear plant model response vs nonlinear plant model response of the current controlled cascaded controller structure. Extended fragment.

In Figure 3.5 and Figure 3.6 the comparison of the systems with linear and nonlinear plant models are presented. Only the force equation varies in the models while the other structure is absolutely the same. Based on the obtained responses it could be observed that both models have equal the rise time and settling time values during the reaction on the initial displacement. However, the nonlinear plant model has the 58% higher overshoot than the linear plant model (0.446 μm and 0.282 μm respectively).

The nonlinear plant model overshoot is 123% higher than the overshoot of the linear plant model (0.382 μm and 0.171 μm respectively). The reaction parameters on the reference position signal are as follows: the linear plant model has monotonous transient response with the settling time value equal to 0.075 seconds, while the nonlinear plant model's overshoot is 15.2% and the settling time is 0.536 seconds. The selected error band is 1 μm.

Summarizing the responses analysis, the linear plant model provides better dynamics, due to the fact that some physical processes (see section 2.1) in the electromagnet coil are neglected, though for more accurate modelling, nonlinear actuator model should be used.

3.4 Inner voltage control

The voltage control block diagram is similar to the one illustrated in Figure 3.4. However, the voltage control is used in the inner control loop. The scaling gain "pu2ph" has the biasing voltage value.

The control methods described in this chapter consist of two control loops, though only the position loop could be used to control the system. However, as could be judged from the responses illustrated in Figure 3.7, the control system comprising two loops has better dynamics than the system with only the position feedback. By the dashed line the system without inner control loop is represented.

Along with the linear force equation, the model based on the nonlinear force equation is also simulated. The models comparison gives the results similar to the inner current control with linear and nonlinear plants.

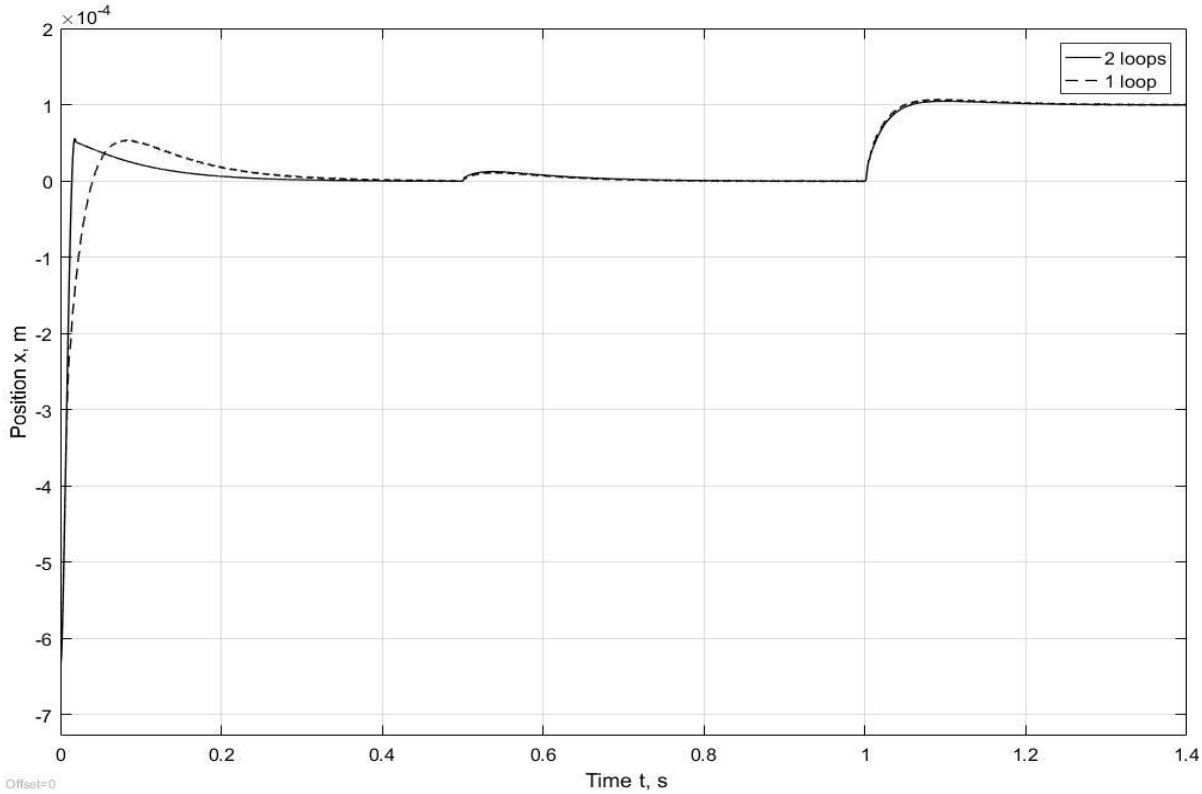

Figure 3.7 Responses of the linear plant systems with 2 loops and 1 loop. The voltage control is applied.

It could be seen that the rise time of the system with one control loop is 2.8 times higher than the two loops system rise time – 0.04 sec and 0.0142 sec respectively. To summarize, the control system with the inner control loop has better dynamics than the system with only position control loop.

3.5 Inner flux control

The inner flux control loop is implemented in the same principle as the current and voltage controls. However, in the flux control system the calculation of the flux should be considered. The equation for the flux calculation is presented by equation 3.2 and is derived in section 4.2.

$$\Phi = \frac{1}{N}\int V\,dt \tag{3.2}$$

The voltage in equation 3.2 is taken by the assumption that the voltage of an electromagnet coil could be measured. The block diagram of the voltage measurement and the flux calculation is presented in Figure 2.2.

The backwards transformation from voltage to flux is performed with the use of the following equation:

$$V = N\frac{d\Phi}{dt} \tag{3.3}$$

The actuator model is illustrated in Figure 2.2. The output gain “pu2ph” has the biasing voltage value, and the control signal transformation is carried out with the subsystem based on equation 3.2. Thus, the control signals from PID controller has the reference flux values, that are fed to the flux controller. Inside the flux controller the reverse transformation is performed to obtain voltage from flux in accordance with equation 3.3. The flux controller structure is shown in Figure 3.8.

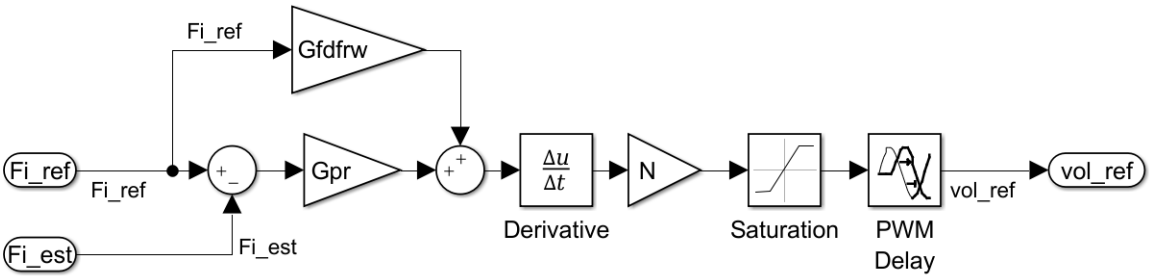

Figure 3.8 Inner flux controller structure.

The controller itself comprises proportional and feedforward gains. The difference between the reference and the estimated flux values obtained from the estimator is fed to the controller. The calculated voltage value from flux is limited with the saturation block and then is delayed to account for the time delay caused by PWM. The flux controller output is the reference voltage that is applied to the electromagnet.

3.6 Control methods comparison

In this section the control principles presented above are compared with each other. Firstly, two loops control systems based on the current, voltage and flux control loops, and with the linear actuator model, are compared. Secondly, systems with the nonlinear plant are discussed, and the responses are presented.

The comparison of the systems' responses is illustrated in Figure 3.9 and Figure 3.10. The rise time, settling time and overshoot values are grouped in Table 3.2 and

Table 3.3. The number in brackets in the settling time column stands for the error band.

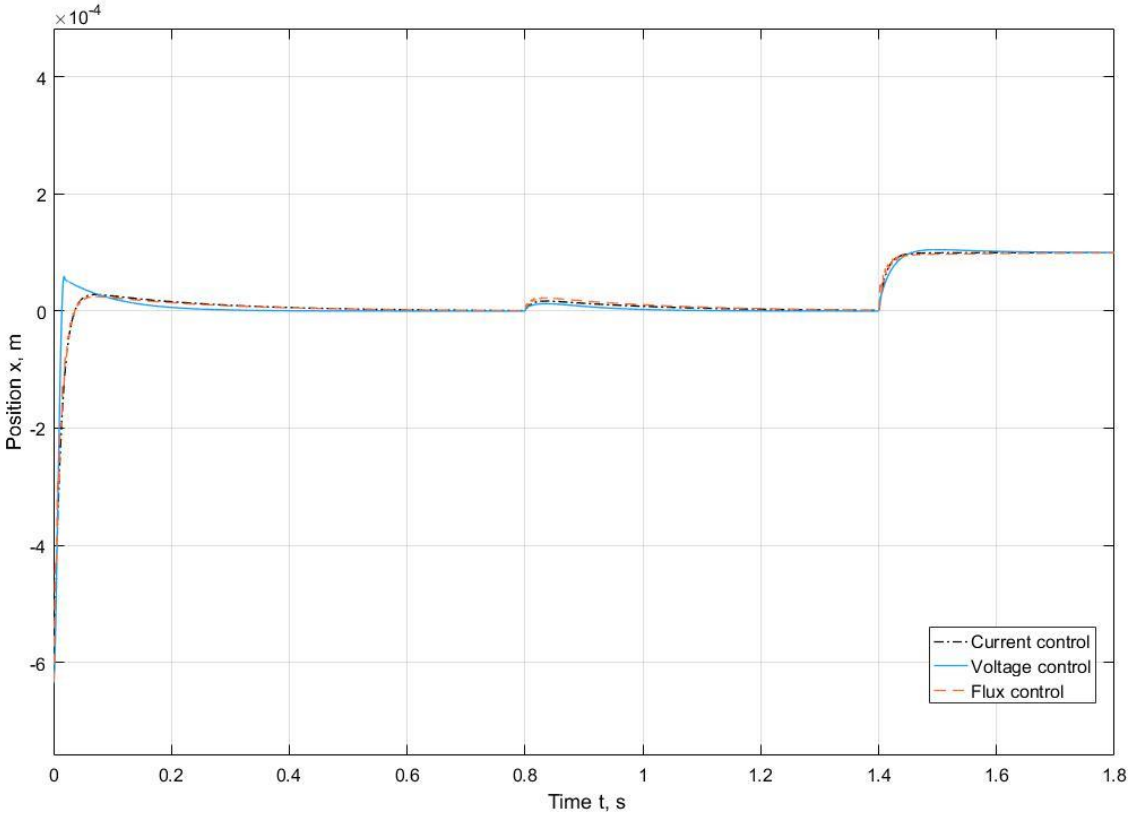

Figure 3.9 Responses comparison of the systems with linear plant.

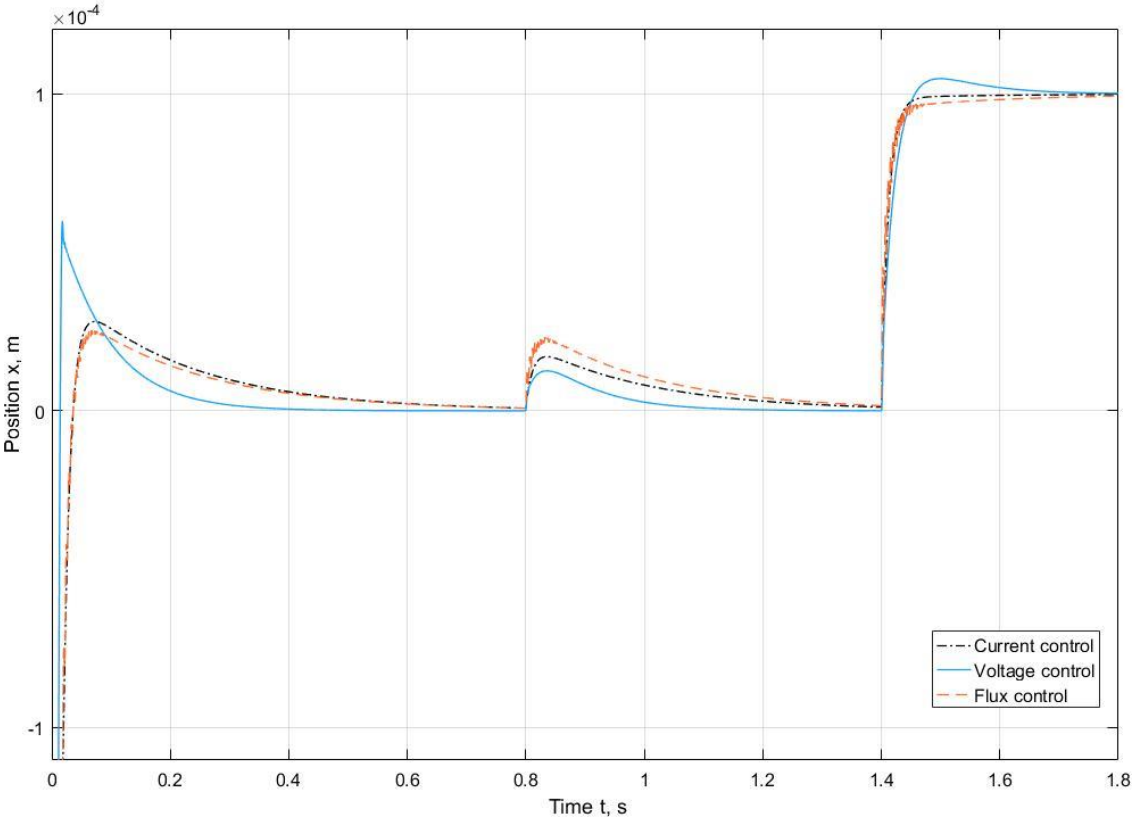

Figure 3.10 Responses comparison of the systems with linear plant. Extended fragment.

Table 3.2 Values of the reactions on the initial displacement

Control method	Rise time, sec	Settling time (10^{-5} m), sec	Overshoot, 10^{-4}m
Current control	0.0217	0.2964	0.2818
Voltage control	0.0095	0.1607	0.5991
Flux control	0.0218	0.2727	0.2542

Table 3.3 Values of the reactions on the constant force disturbance

Control method	Settling time ($5 \cdot 10^{-6}$ m), sec	Overshoot, 10^{-4}m
Current control	0.298	0.1709
Voltage control	0.144	0.1262
Flux control	0.359	0.2333

The voltage control has the smallest rise time and settling time values, though the overshoot is nearly 2 times higher than the other control principles overshoot. Based on the figures and the table presented above the current and the flux control have the similar dynamics. However, the overshoot in the system with the flux control is 10% lower than the current control systems, but at the same time the flux control has oscillations, that could be neglected.

The reaction on the constant force disturbance applied are grouped in the Table 3.3. Judging by the parameters' values in Table 3.3, the best dynamics of the reaction on the constant force disturbance are achieved with the voltage control principle. In contrast, the voltage control is the only control principle studied that has the overshoot after the reference signal application. The best dynamics in following the reference signal are obtained by the current control principle. It is arguable to highlight the best control option among the studied principles, as the trends in the reactions are different on the signal and disturbance applied. However, the comparison points are mentioned above.

3.7 Nonlinear control principles comparison

In this section the comparison of the systems with the nonlinear actuator model is presented. It should be mentioned that the system with the inner flux control loop is unstable if the actuator is represented by the nonlinear model. With such an actuator model a model-based and/or nonlinear controller should be designed. Thus, only the inner current and the inner voltage controls are compared. The comparison of the systems' responses is illustrated in Figure 3.11 and Figure 3.12. The values of the rise time, settling time and the overshoot are grouped in Table 3.4 and Table 3.5.

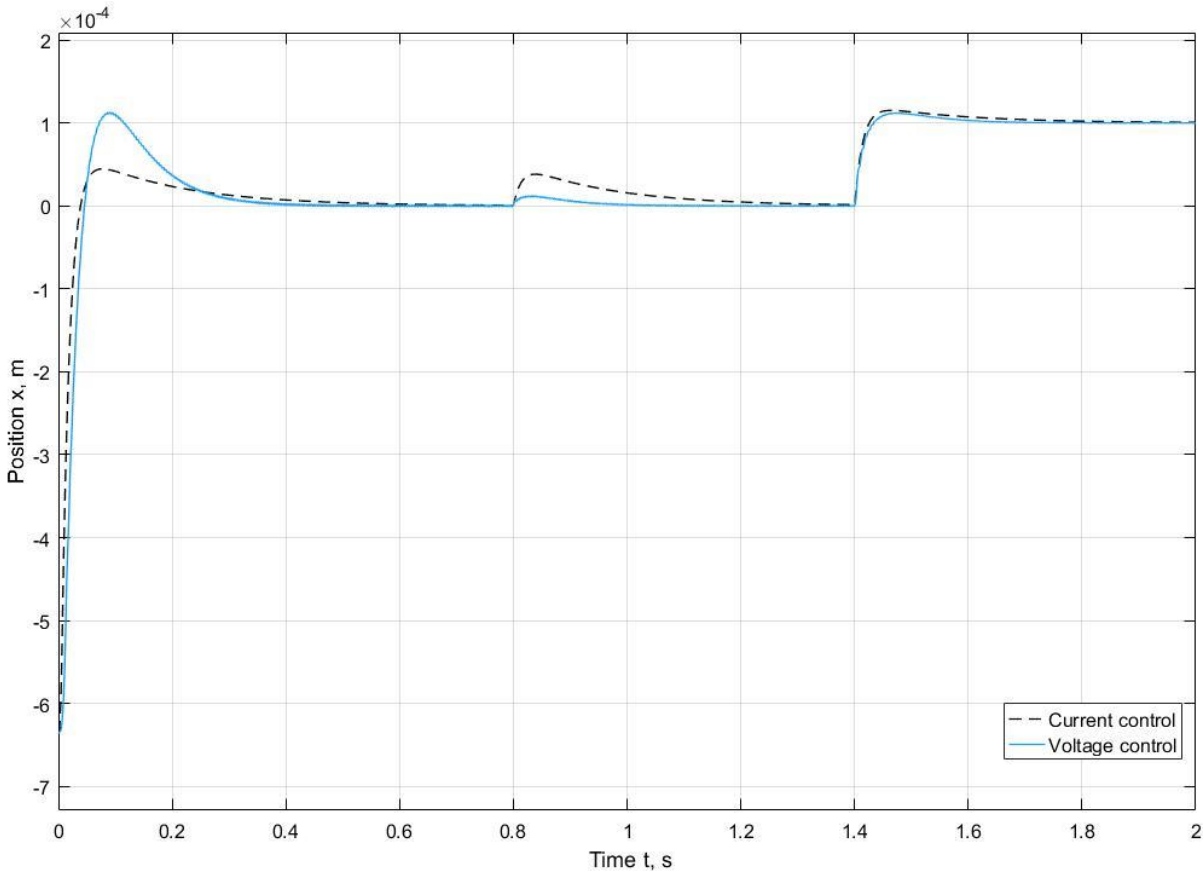

Figure 3.11 Responses comparison of the systems with nonlinear plant.

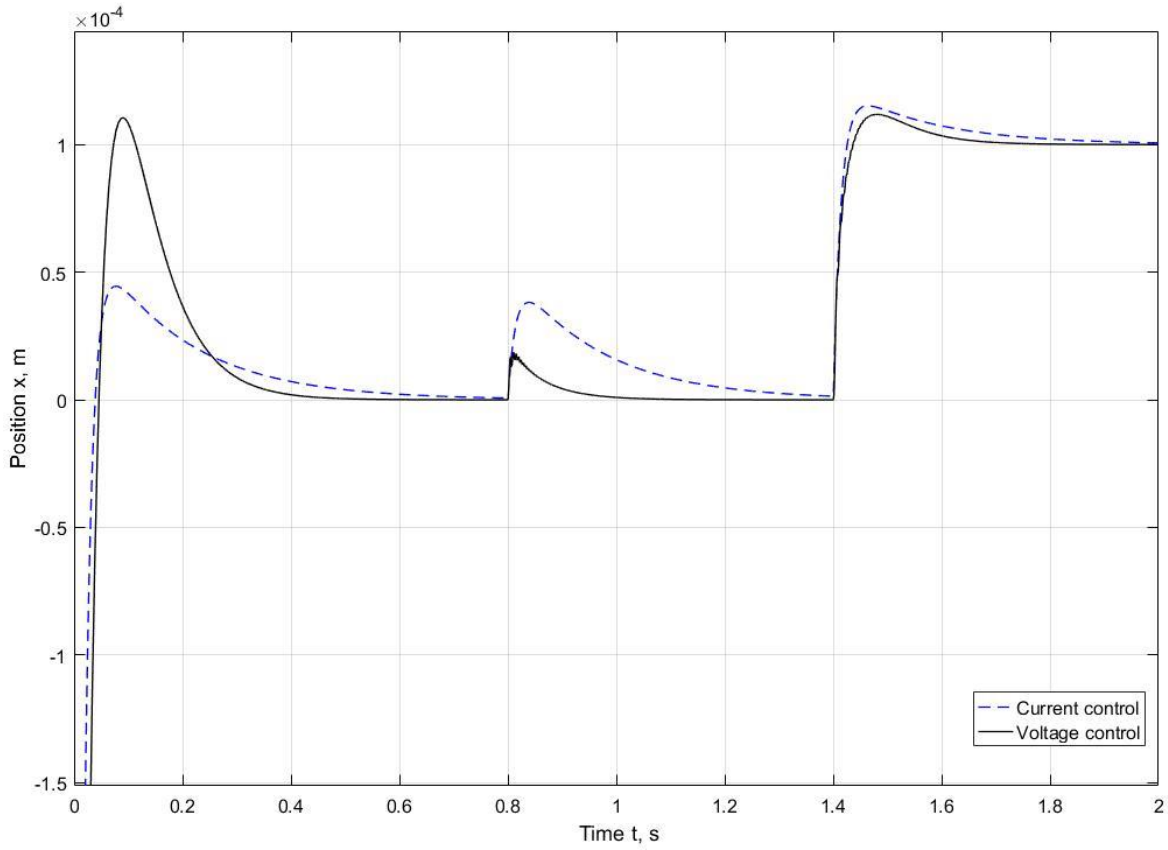

Figure 3.12 Responses comparison of the systems with nonlinear plant. Extended fragment.

Table 3.4 Values of the reactions on the initial displacement

Control method	Rise time, sec	Settling time (10^{-5} m), sec	Overshoot, 10^{-4}m
Current control	0.0233	0.3431	0.441
Voltage control	0.0283	0.2908	1.106

Table 3.5 Values of the reactions on the constant force disturbance

Control method	Settling time ($5 \cdot 10^{-6}$ m), sec	Overshoot, 10^{-4}m
Current control	0.389	0.381
Voltage control	0.092	0.186

Examining the responses and the tables it could be summarized that the voltage control with the nonlinear actuator model has better dynamics than the current control, though its

overshoot in the reaction on the initial displacement is 2.5 times higher (251% higher). Accounting for the overshoot, the voltage control has the 15% lower settling time.

Based on the reactions on the constant force disturbance the better dynamics are achieved with the voltage control loop, as the overshoot is 2 times lower, and the settling time is 4.2 times faster. However, it should be considered that the voltage control response has oscillations, that could be neglected though. The reactions on the reference signal applied are approximately the same, but the current control system's overshoot is 3% higher.

To summarize, the voltage control provides better dynamics performance, as when the reaction on the initial conditions is over (the rotor lift-up is completed), the system's reaction on the force disturbances and the reference position signal are very important, thus, the inner voltage loop is considered to be the most suitable among the simulated.

3.8 Summary

The chapter is focused on the conventional magnetic bearing control principles. The control systems with two control loops were studied, and the responses compared. Both the linear and nonlinear actuator models were simulated. Based on the simulation results, the inner voltage control loop is considered to be the most suitable control principle for the nonlinear plant system with two loops among the studied.

4. DIRECT FORCE CONTROL

In general, in AMB control systems the electromagnet coil current is used as a control variable. However, the coil current usage for a AMB state definition has several drawbacks as follows: unstable zero; stray flux and eddy currents could be lost; nonlinear relation of the current with the airgap and generated magnetic force [14].

In this chapter the control method, that based on the direct control of the electromagnet force is presented. In accordance with the previous researches [8,14], the control method eases the modeling of non-ideal AMB parameters and provides more linear behavior.

The main advantage of the DFC principle is the inner control loop absence. The presented control method could considerably increase the response speed of the system and, thus, to make a system more controllable. In addition, as the voltage is applied to the electromagnets in the form of voltage vectors, there is no need for the PWM, thus, there is no corresponding time delay. In analogy with the DTC in electrical drives, the control variables are obtained directly from the control object [17].

4.1 Direct torque control

In the DTC principle, the controlled variables are represented by the magnetizing flux and the motor torque. The calculation of the motor magnetic flux and the torque values is based on the measured voltage and current values of the motor.

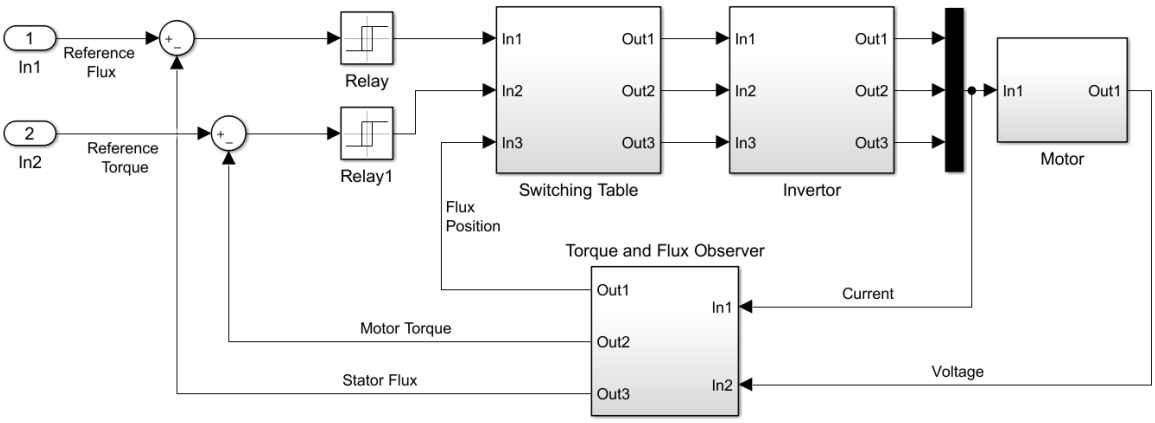

Figure 4.1 DTC drive diagram.

For the stator flux linkage calculation, the stator voltage is integrated. The torque value is obtained from the estimated flux linkage value and the measured motor current vector. The obtained flux and toque values are compared with the reference values, as illustrated in Figure 4.1. If the difference between the estimated and the reference values is more than the selected tolerance, the corresponding voltage vector is applied to eliminate the error between the reference and the estimated value [18-20]. In [18-20] the voltage vectors and the switching table are presented and discussed. The voltage vectors are selected in accordance with the switching table to keep the error between the reference and the estimated value within the selected error band in the form of hysteresis. In AMB control systems the corresponding principle could be adapted for the direct force control, in which the voltage vectors, selected in accordance with the switching table, are used to keep the force value in the tolerance band.

In comparison with field-oriented control (FOC) or vector control, in the DTC technique motor variables are controlled directly, thus there is no need for a modulator in a drive.

In addition, speed and position sensors are unnecessary, what results in a DTC drive, that is 10 times faster than other control principles of AC or DC drives. Speed accuracy is estimated to be 8 times better than other AC drive with the open-loop control scheme [17]. The DTC drive response is considerably faster than PWM drive because of the modulator absence.

4.2 Mathematical model

In accordance with the AMB equations, the force generated by the electromagnet is a function of the voltage applied to the electromagnet coil. Based on Maxwell equation (4.1), the magnetic field strength could be expressed as in (4.2), (4.3):

$$\nabla \times \boldsymbol{H} = \boldsymbol{J} + \frac{\partial \boldsymbol{D_e}}{\partial t} \tag{4.1}$$

where $\boldsymbol{H}, \boldsymbol{J}, \boldsymbol{D_e}$ are the magnetic field strength, current density and electric flux density respectively.

$$\sum_{\forall i} I_i = \oint_S \boldsymbol{H} d\boldsymbol{s} \tag{4.2}$$

(4.3)

$$NI = 2l_{air}H_{air} + l_{core}H_{core} + l_{thr}H_{thr},$$

where l – the magnetic line length in the circuit corresponding part. Indices *air*, *core* and *thr* indicates the parts of the axial AMB circuit: the airgap, electromagnet core and thrust disc respectively. The magnetic line path is illustrated in Figure 4.2.

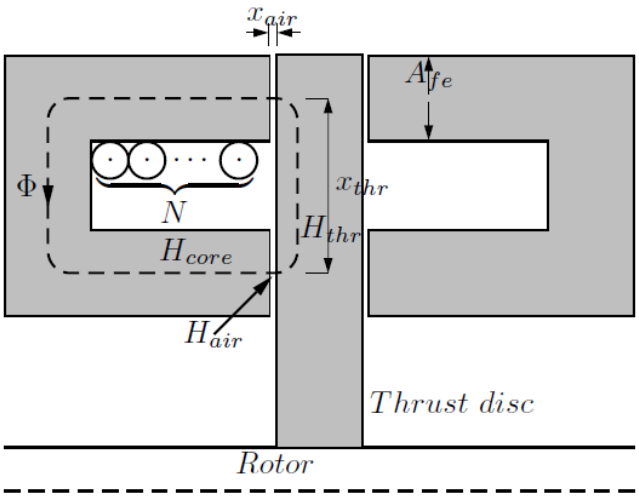

Figure 4.2 Magnetic line path in axial AMB electromagnet. [14]

The integral in equation 4.2 comprises three parts, though the magnetic force in the airgap should be considered. Assuming, that the field density Φ/S_{air} is constant in the electromagnet pole area S_{air}, the current in the airgap could be expressed as follows:

$$I_{air} = \frac{2l_{air}}{N}H_{air} = \frac{2l_{air}}{N\mu_0 S_{air}}\Phi \tag{4.4}$$

With the use of Faraday's law and equation 4.4, magnetic energy W in the airgap could be calculated:

$$W = \int \frac{d\Phi}{dt} NI_{air} = \frac{l_{air}}{\mu_0 S_{air}}\Phi^2 \tag{4.5}$$

From the equation (4.5) the force could be obtained:

$$F = \frac{W}{x} = \frac{1}{\mu_0 S_{air}}\Phi^2 \tag{4.6}$$

Thus, the required voltage V_w for the force F generation is expressed as follows:

$$\Phi = \frac{1}{N}\int V\,dt \tag{4.7}$$

$$V_w = N\sqrt{\mu_0 S_{air}}\frac{d}{dt}\sqrt{F} \tag{4.8}$$

Equation 4.8 allows to calculate the force in a magnetic bearing by the integration of the applied voltage V_w, or to calculate the required voltage value to provide the desired force. Based on the equations, unlike the current control, in the force control there is no need to compensate the varying airgap value. The presented control method is used in the magnetic flux control or voltage control of AMB [14].

Practically, there is a number of effects that could lead to inaccuracies occurrence in the flux estimation based on the integration of the voltage applied to an electromagnet. The inaccuracies are caused by [14]:

- Losses in cables, coils;
- Amplifier dead times;
- Eddy currents;
- Stray fluxes;
- Electrical and magnetic coupling between axes.

Thus, instead the flux calculation, it could be measured with the use of flux sensors. For instance hall sensors could be used, though several drawbacks are stated:

- Additional wires in the system;
- Additional sensors make the system more complex and expensive;
- Additional dead-time leading to the phase losses increment.

In the designed control principle, the flux estimator based on equation 4.7 is used to obtain the flux value.

4.3 Control principle

The control principle in the designed DFC is implemented by two control loops – the outer position control loop and the inner control loop. The outer position control is based on the

PID controller, to the input of which the difference of reference position signal and measured airgap value is transmitted. The output of the controller is the reference force value F_{ref}. In Figure 4.3 the DFC block diagram is presented.

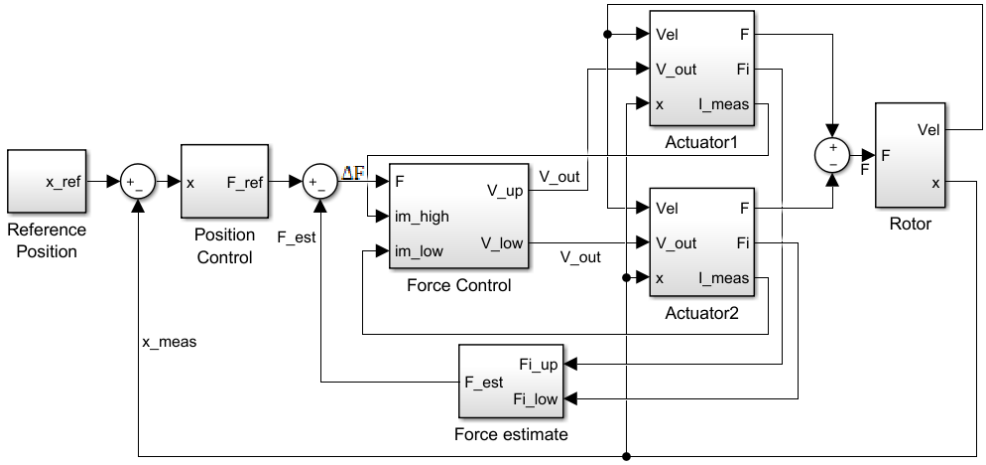

Figure 4.3 DFC block diagram.

The difference of the reference force value F_{ref} and the estimated force value F_{est} is called ΔF.

$$\Delta F = F_{ref} - F_{est} \tag{4.9}$$

The inner control loop is implemented as the switching table. The ΔF is fed to the switching system, where its value belonging to one of the ranges is determined. In accordance with the ΔF value interval, the voltage vector is selected, and the voltage $U_{DC} \in \{-150\ V, 0, 150\ V\}$ is applied to the electromagnets.

By equation 1.13 the forces produced by electromagnets are calculated as shown in Figure 2.2 and then are summed with the opposite signs to get the force generated by the pair of two opposite electromagnets.

The estimated force value is obtained with the use of the estimator based on equation 4.6. The estimator block diagram is illustrated in Figure 4.4.

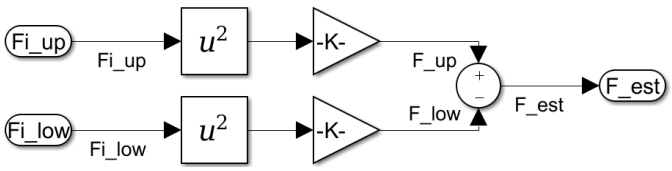

Figure 4.4 Force estimator block diagram.

The control system was also tested without the estimator, and the response has considerable oscillations around the operation position, and the system follows the reference position signal with a high steady state error value. Thus, the estimator is necessary to fulfill the control requirements.

The estimator is based on the inputted electromagnets flux value (in Figure 4.4 Fi_up and Fi_low represents the upper and lower electromagnets flux value respectively), that are used in the calculation in accordance with equation 4.6. The difference of the forces generated by two opposite electromagnets represents the estimated force value of the electromagnets pair acting along the same axis. The calculated force value is used in equation 4.9 as discussed before.

Figure 4.5 illustrates the ranges according to which the voltage vectors switching is performed. The vertical axis represents the voltage vectors as shown in Figure 4.6, the horizontal axis indicates the ΔF levels. The levels values are grouped in Table 4.1.

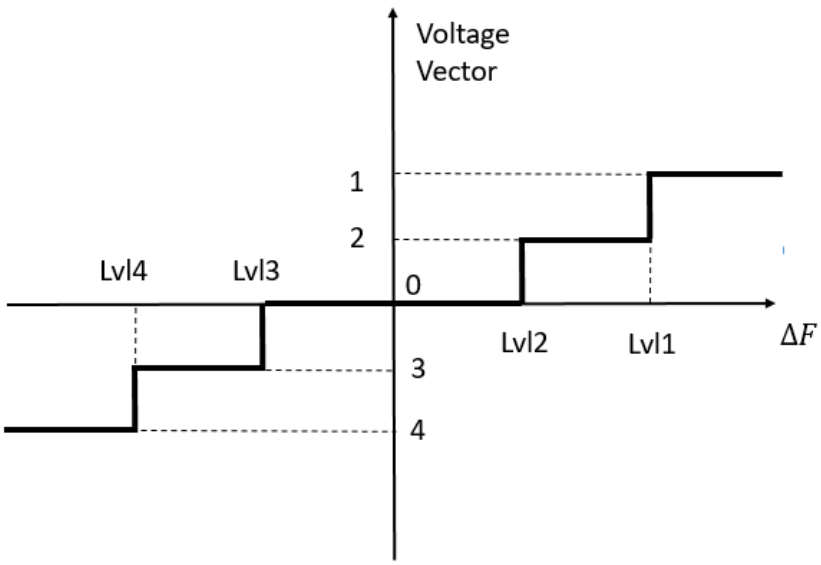

Figure 4.5 Switching diagram.

Table 4.1 Switching diagram levels values

Level	Value, N
Lvl1	300
Lvl2	30
Lvl3	-30
Lvl4	-300

In Figure 4.6 the voltage vectors represent the voltage to be applied to two opposite electromagnets acting along the same axis. The voltage applied to the electromagnet coil could be either positive, negative or zero, what is represented by 1, -1 and 0 respectively. Two numbers in parenthesis stands for the first and seconds electromagnets acting along the same axis.

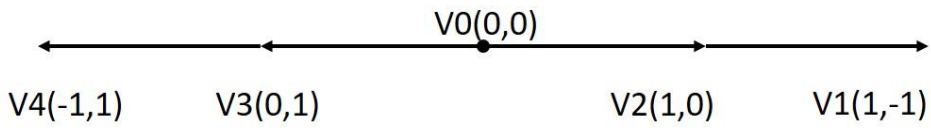

Figure 4.6 Voltage vectors.

The logic of the several levels implementation is justified with the assumption, that under the conditions of relatively high displacement from the reference position value, two electromagnets are acting at the same time to speed up the process of stabilizing the system, while during the relatively small displacement only one electromagnet force is enough. In addition, for more stable operation a dead zone is set between the levels 2 and 3. The zero-voltage vector is related to the dead zone, thus the voltage is not applied to the electromagnets if the ΔF value is in the dead zone.

The electromagnets configuration in relation to the ΔF value is presented in Table 4.2.

Considering the fact, that the current in the electromagnet coil should not be less than zero, the switching logic includes the principle of checking the measured current value. Under the condition of the current value being less than 0.1 A, the voltage is not applied to the corresponding electromagnet. Thus, during some time intervals the voltage vector 1 and the vector 4 are replaced with the vectors 2 and 3 respectively.

Table 4.2 Switching Table

Interval	Upper Electromagnet	Lower Electromagnet	Voltage Vector
$L_3 < \Delta F < L_2$	0	0	0
$\Delta F > L_1$	1	-1	1
$L_2 < \Delta F < L_1$	1	0	2
$L_4 < \Delta F < L_3$	0	1	3
$\Delta F < L_4$	-1	1	4

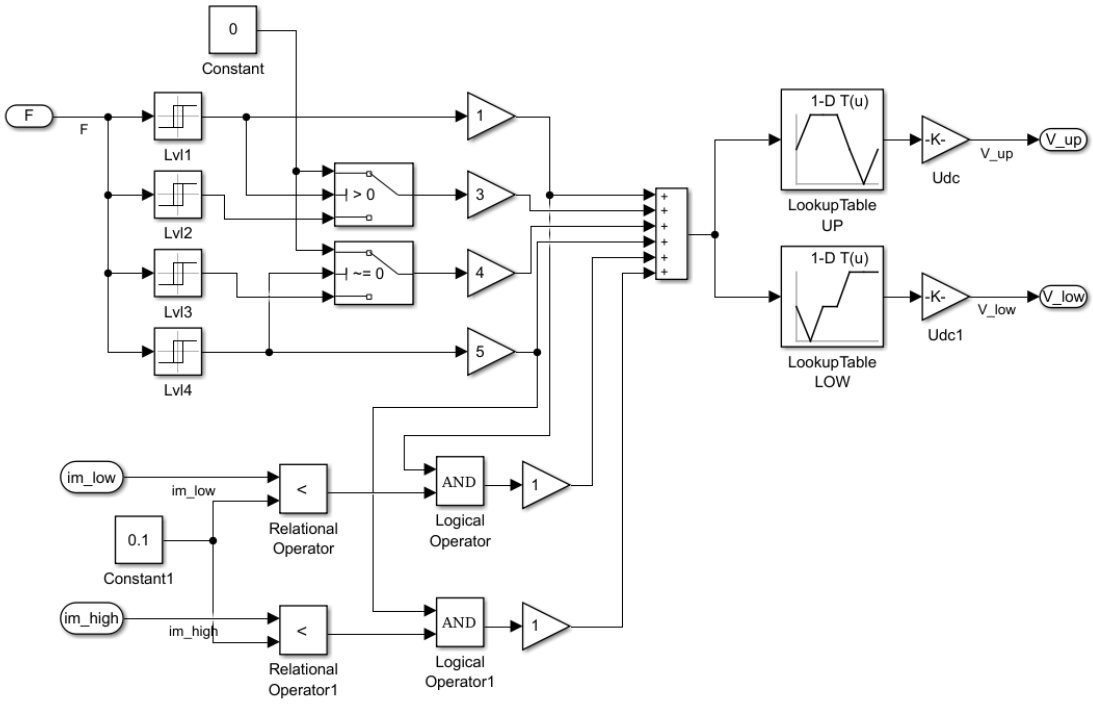

Figure 4.7 Force control subsystem.

Figure 4.7 illustrates the force control subsystem structure. By the saturation blocks Lvl1 – Lvl4 the switching diagram as in Figure 4.5 is implemented. Two relational operators are used for checking the conditions of coil current being no less than some small value selected. Even though in some conditions the force range is on the level 1 or 4 (Figure 4.5), if the coil current is close to zero, another voltage vector is switched. The lookup table blocks are used to output one of the voltage configurations – positive, negative or zero.

4.4 Simulation results

In this section the model simulation of the block diagram presented in Figure 4.3 is presented. The system was tested on the conditions and disturbances presented in section 2.3. The response is depicted in Figure 4.8, and the voltage vectors switching is illustrated in Figure 4.9. The switching levels shown in Figure 4.5 have the values listed in the Table 4.1.

Analyzing the response in Figure 4.8, the rise time is 0.0158 seconds, and the oscillations are within the range of $-0.25 * 10^{-5} \div 0.25 * 10^{-5}$ meters, what is neglectable.

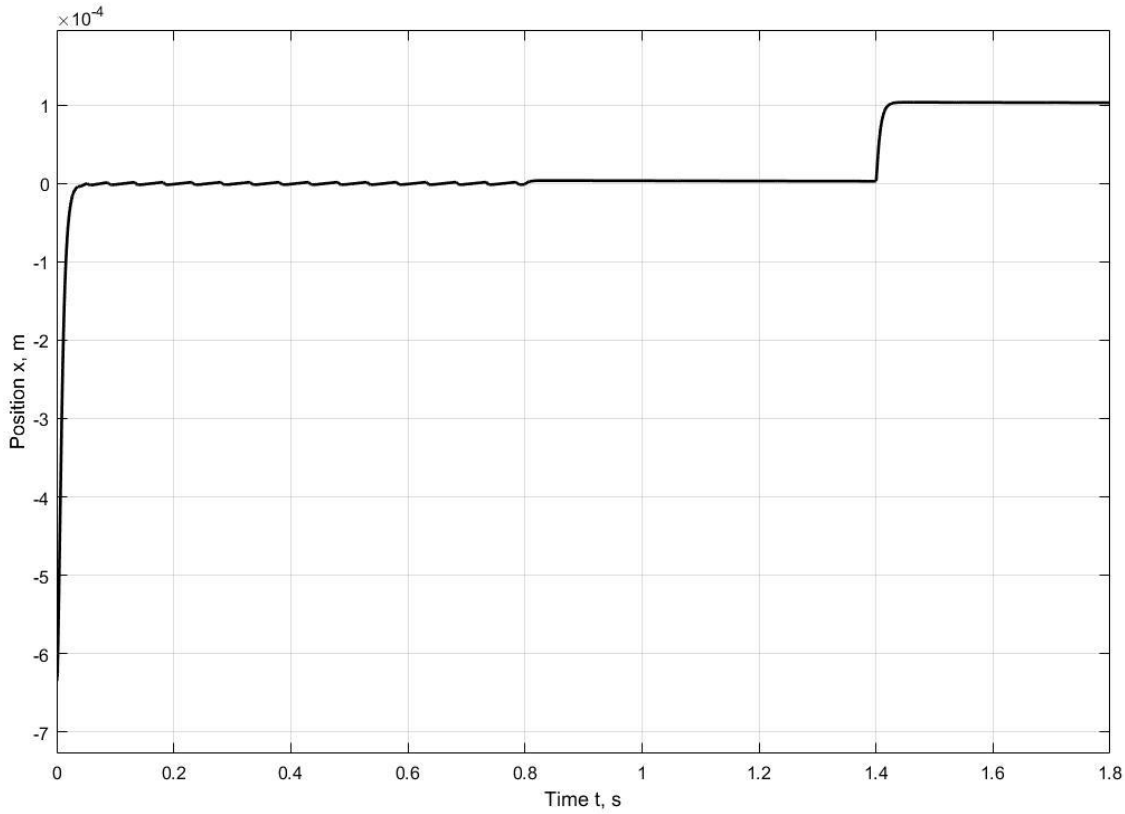

Figure 4.8 Response of the nonlinear system on the disturbances.

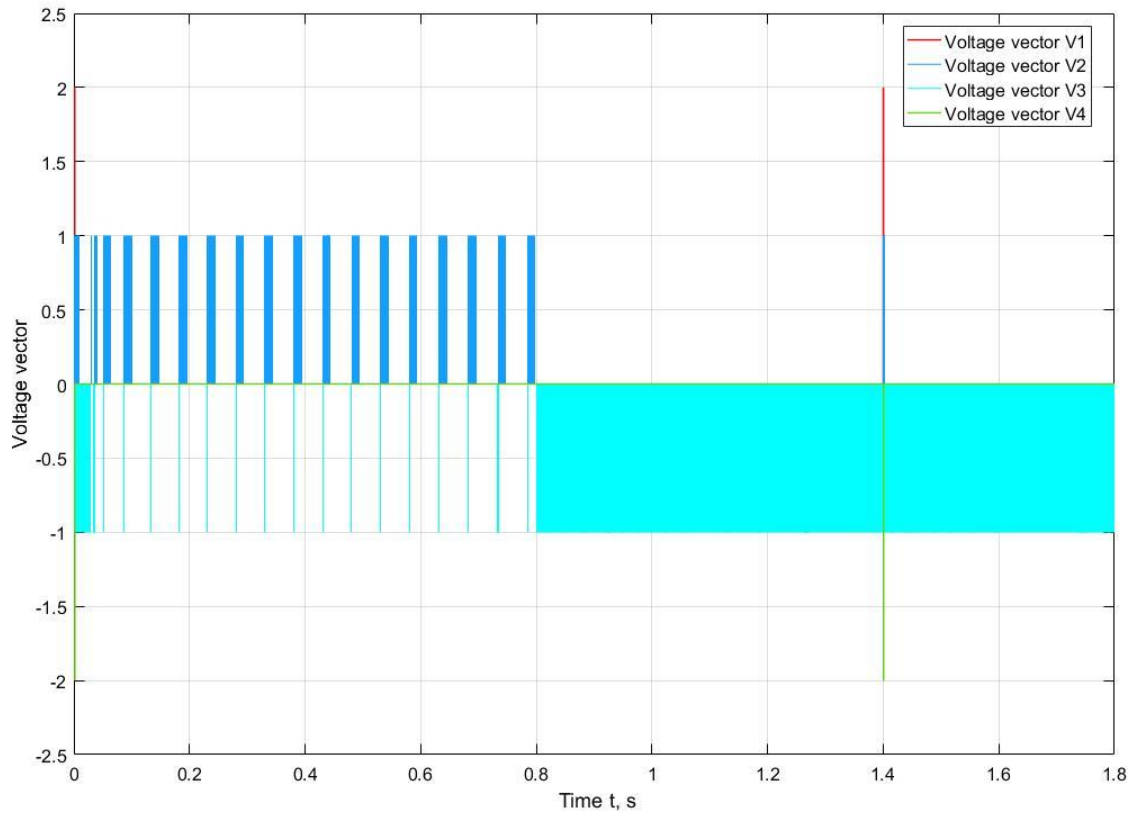

Figure 4.9 Voltage vectors switching.

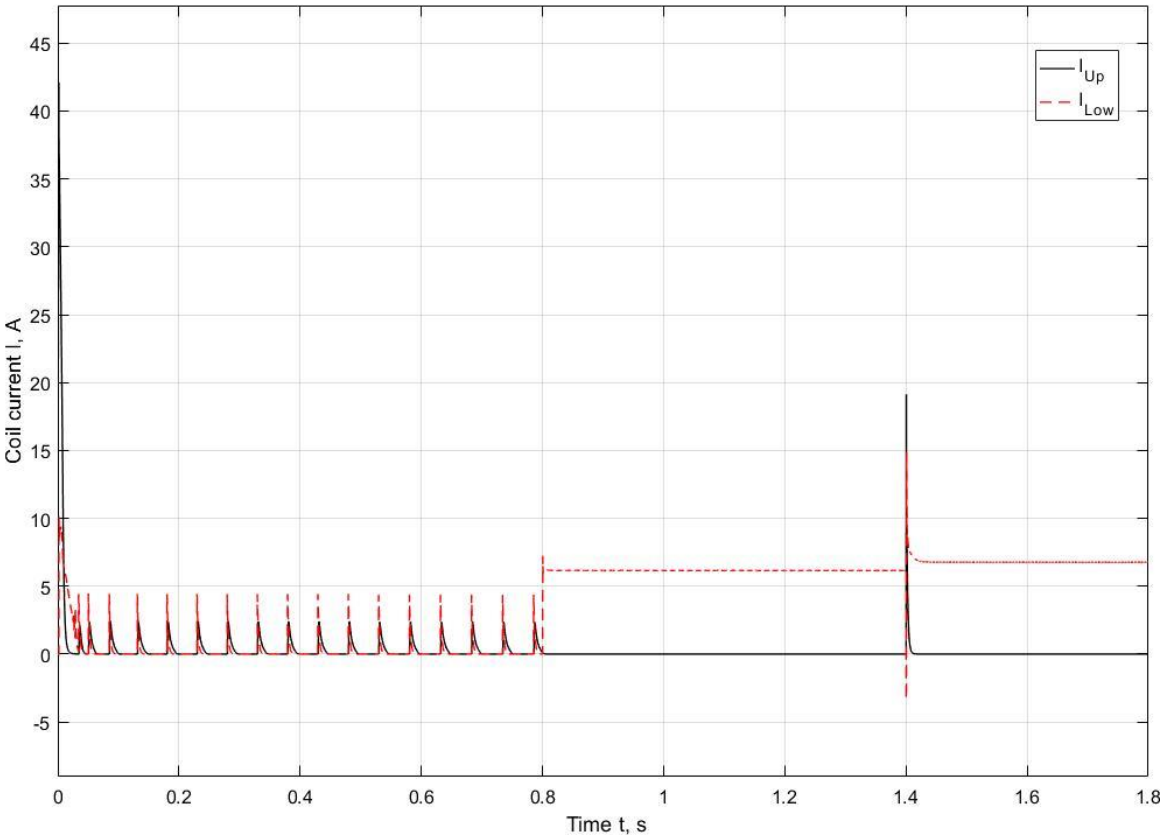

Figure 4.10 Measured coil currents diagram of upper and lower electromagnets.

The oscillations exist until the force disturbance is applied. As the constant force is applied, there is a small steady state error with the value going down from $0.3 * 10^{-5}$ to $-0.23 * 10^{-5}$ meters.

The refence signal applied comes to the steady state in 0.04 seconds with the error of 3 μm, what is considered as a neglectable error.

By the spikes in Figure 4.9 the electromagnets voltage vectors (see Figure 4.6) are represented. The spikes that are above the x-axis represents the upper electromagnet, the lower electromagnet voltage is shown by the spikes below the x-axis. Spikes that have the value of 2 and -2 represent the two electromagnets acting simultaneously. As could be observed from the response presented in Figure 4.8 during the time periods, when the displacement is relatively high, both electromagnets have the voltage applied, otherwise only one electromagnet is acting to eliminate the displacement.

The measured coil currents diagram is illustrated in Figure 4.10. During the reaction on the initial displacement the currents are characterized with the spikes. After the end of the

transient response (the rotor position is close to the zero value), there are constant switches that could be observed in Figure 4.8 and Figure 4.9 as well, thus the currents spikes appear. Under the condition of the applied force disturbance and the reference signal (see section 2.3), one of the electromagnets has the constant current value to oppose the disturbances.

The control dependence on the switching levels values was also studied. If the Level 2 value is decreased (the Level 3 value is increased, as the levels are symmetrical with respect to the *x* axis), more switches between the voltage vectors occur and, thus, the oscillations before the constant signal application have higher frequency. To summarize the variation of Levels 2 and 3 parameters, the closer the values to zero, the higher the number of switches and, thus, the frequency of the oscillations is also higher. In Figure 4.11 the response of the nonlinear system with the changed switching levels values (see Table 4.3) is illustrated.

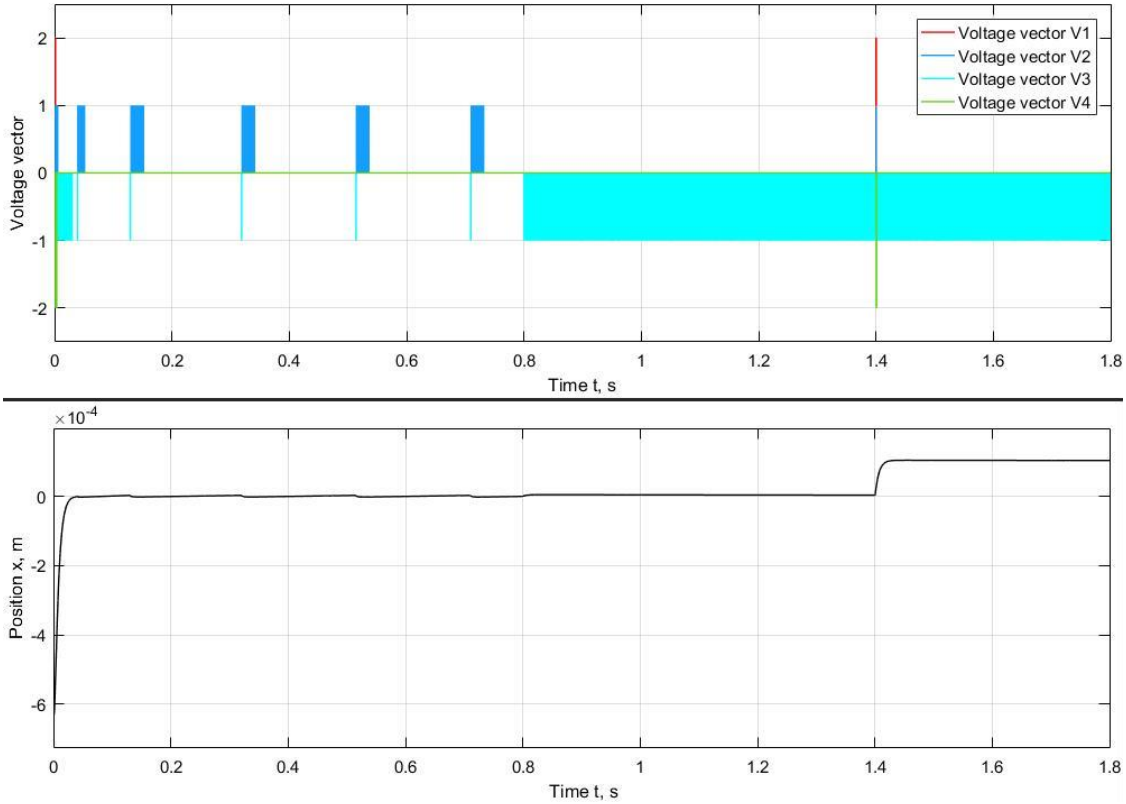

Figure 4.11 Response of the nonlinear system with higher switching levels values on the disturbances.

The switching levels in the simulation with the changed parameters has higher values (see Table 4.3 and Table 4.1) than in the simulation with the results illustrated in Figure 4.8 and Figure 4.9. Thus, the number of switches is lower, what could be observed in Figure 4.11.

Table 4.3 Switching diagram levels' values

Level	Value, N
Lvl1	350
Lvl2	50
Lvl3	-50
Lvl4	-350

The rise time values of the systems with different switching levels are the same and have the value of 0.0158 sec. The dynamic performance values are listed and compared with other control principles in section 4.5.

The sampling time decrease from $100\ \mu s$ to $1\ \mu s$ reduces the number of switches, and the response oscillations are nearly eliminated, though it does not affect the response on the constant disturbance and reference signal applied. Thus, the sampling time reduction causes the system to be more stable.

4.5 Comparison with other control principles

To evaluate the perfection of the DFC principle the system response is compared with the responses obtained in the chapter 3. For a fair comparison, all the control principles are based on the nonlinear actuator model. In addition, the DFC principle has two control loops: the outer position control loop and the inner force control loop. The sampling time and the signals applied are the same for all the models. The DFC model in the simulation has the switching levels values presented in the Table 4.1.

The responses are illustrated in Figure 4.12 and Figure 4.13. The parameters values are composed in Table 4.4 and Table 4.5.

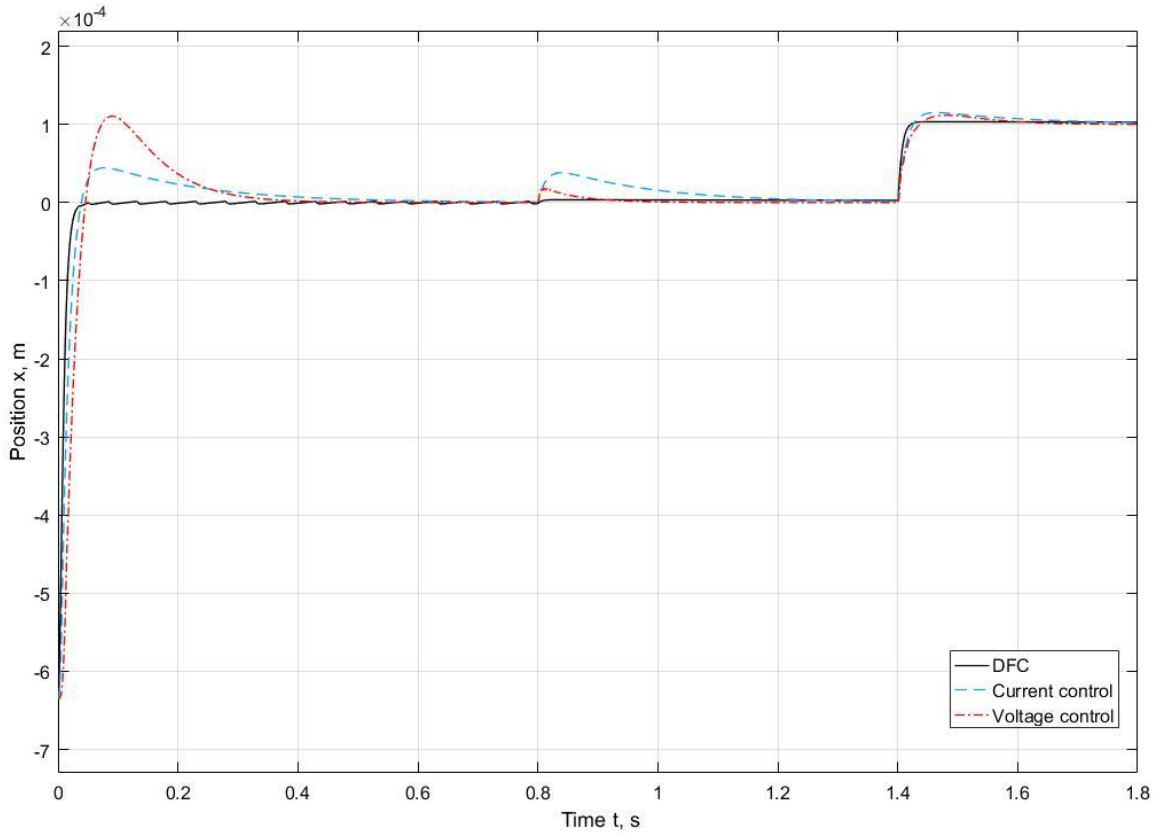

Figure 4.12 Responses comparison for the nonlinear plant model.

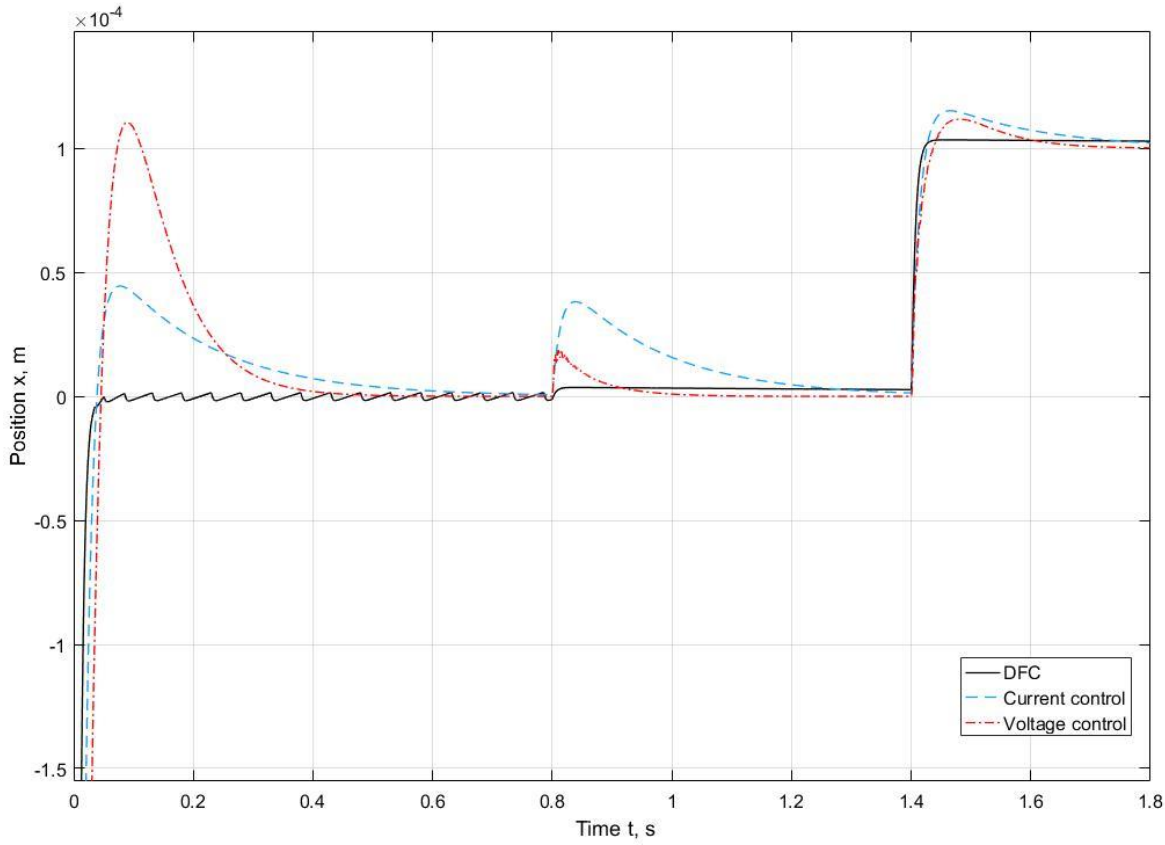

Figure 4.13 Responses comparison for the nonlinear plant model. Extended fragment.

Table 4.4 Values of the reactions on the initial displacement

Control method	Rise time, sec	Settling time (10^{-5} m), sec	Overshoot, 10^{-4}m
DFC	0.0158	0.0298	0
Current control	0.0233	0.3431	0.441
Voltage control	0.0283	0.2908	1.106

Table 4.5 Values of the reactions on the constant force disturbance

Control method	Settling time ($5 \cdot 10^{-6}$ m), sec	Overshoot, 10^{-4}m
DFC	0	0
Current control	0.389	0.381
Voltage control	0.092	0.186

In addition to the values presented in the tables above, DFC provides the reference signal response with the zero-value overshoot. However, the steady state error of 3 μm exists, though it is considered as a neglectable error.

The comparison of the responses allows to prove that the DFC principle could significantly reduce the system reaction time and provide the following of the reference signals and disturbances without any overshoot.

The designed control principle is more optimal in terms of energy consumption, as during the periods of relatively small rotor displacements only one electromagnet is acting instead of two in the differential driving mode. Two opposite electromagnets are activated only when the displacement value is high, what is illustrated in Figure 4.9.

4.6 Summary

In this section the DFC principle was designed. All the necessary equations were derived and discussed. The methods to obtain the flux value were introduced, and then the estimator selection was justified. The voltage vectors, switching table and switching logic were introduced in section 4.3. The response dependence on the switching levels values and the sampling time value was studied. Then the simulation results were presented and compared with the other control principles results.

By the responses obtained during the simulation, the superiority of DFC over the conventional control principles was justified. The rise time, settling time and overshoot values are significantly better than the other methods.

CONCLUSION

In the first chapter, the background information was presented – the AMB operation principle, applications, advantages and drawbacks of the technology. The AMB-rotor system structure was introduced and discussed, the radial force generation principle was presented, and the force equation for a single electromagnet was derived. Later, more complex equation for the magnetic bearing force and the pair of electromagnets was derived. The rigid rotor model was described with the set of equations, the various actuator dynamics approximations were presented, and the corresponding Bode plot was plotted.

In the second chapter, the magnetic actuator block diagram was presented and explained, and the PWM used in the AMB-rotor system was introduced and described shortly. The nonlinear magnetic actuator behavior was explained, and the equations for the actuator dynamics were derived. Based on the presented equations the nonlinear electromagnet model was designed, and the rotor model as a point mass was illustrated. The differential driving mode for AMB was explained. In addition, the reference signal and disturbances applied to the system to test its performance were introduced, and the values of parameters used during the simulation were specified.

In the third chapter, the magnetic bearing control is studied. The general control structure of the AMB-rotor system with two control loops was presented and discussed. The PID controller used as the outer position controller was presented, and its parameters were introduced. To make the control principles comparable the outer position controller is the same for all the inner loops. The inner current, voltage and flux control loops were studied; both linear and nonlinear actuator dynamics were examined. For the current control the comparison of the linear and nonlinear plants was presented, and the linear actuator model provides better dynamics due to the neglection of some physical processes in the electromagnet coil. For the voltage control the system with two loops was analyzed along with the system with the outer position control only. The responses clearly show that the two loops system provides better dynamics. However, for the flux control only the linear actuator model was studied, as the system with nonlinear plant is unstable, and the model-based controller is needed. Later, all the control principles were compared with each other. The decision about the best control principle of the system with linear dynamics is arguable, while for the nonlinear actuator dynamics the voltage control provides better response.

In the fourth chapter, the direct force control is studied. The DFC principle is based on the direct torque control principle in electrical machines and drives. The advantages of DFC over the conventional magnetic bearing control were mentioned. As a design step, the mathematical model was derived, and the flux estimator was designed. The flux estimator selection instead of a flux sensor was justified. Later, the control principle was presented: the voltage vectors were introduced, the switching logic and switching table were presented. In addition, the limitations on the coil currents were discussed and implemented in the control method. The DFC response was compared with the results obtained in the third chapter, and the corresponding analysis was presented.

The DFC provides the best dynamics among the studied control principles. The rise time, settling time and overshot values are significantly better than those of other simulated control principles. The ability to operate either with two opposite electromagnets simultaneously or with only one electromagnet allows to apply voltage to the magnet only when it is needed and, thus, to optimize the response time and energy consumption. Due to the voltage being applied to electromagnets is in the form of voltage vectors, the PWM is not needed, thus, the time delay caused by it is eliminated, and the model is simpler. By the force values selection for the switching levels the control could be adapted for the specific needs – the number of switches is dependent on the force levels values.

The further work on the thesis comprises the following steps:

- Flexible rotor consideration;
- Estimator of the electromagnet coil voltage design;
- PWM implementation;
- The model based controller for the flux control design;
- Laboratory tests conduction for the DFC.

REFERENCES

1. Chiba, A., Fukao, T., Ichikawa, O., Oshima, M., Takemoto, M., Dorrell D.G., Magnetic Bearings and Bearingless Drives, Newnes, USA, 2005.
2. Schweitzer, G., Maslen E.H., Magnetic bearings. Theory, design, and application to rotating machinery, Springer, Switzerland, 2009.
3. Chen, W.J., Gunter, E.J., Introduction to Dynamics of Rotor-Bearing systems. Trafford publishing, Victoria, Canada, 2005.
4. Jastrzebski, R.P., Design and implementation of FPGA-based LQ control of active magnetic bearings. Doctoral thesis, Acta Universitatis Lappeenrantaensis 296, LUT, Finland, 2007.
5. Wassermann, J., Schulz, A., Schneeberger, M., Active Magnetic Bearings of High Reliability, *IEEE International Conference on Industrial Technology*, Vol. 1., 2003, pp. 194-197.
6. Hynynen, K., Broadband excitation in the system identification of active magnetic bearing rotor systems. Doctoral thesis, Acta Universitatis Lappeenrantaensis 446, LUT, Finland, 2011.
7. Boehm. J., et al., Sensors for magnetic bearings, *IEEE Transactions on Magnetics 29*, Part 2, 1993, pp. 2962–2964.
8. Lösch, F., Identification and automated controller design for active magnetic bearing sytems. Doctoral thesis, ETH Zürich, Switzerland, 2002.
9. Genta, G., Dynamics of Rotating Systems, Springer, New York, 2005.
10. Lantto, E., Robust control of magnetic bearings in subcritical machines. Doctoral thesis, Helsinki University of Technology, Finland. EL 94., 1990.
11. Zhang, J., Karrer, N., IGBT power amplifiers for active magnetic bearings of high speed milling spindles, *Proceedings of the 1995 IEEE IECON 21st International Conference*, Vol.1., Orlando, FL, USA, 1995, pp. 596-601.
12. Hutterer, M., Schrödl, M., Control of Active Magnetic Bearings in Turbomolecular Pumps for Rotors with Low Resonance Frequencies of the Blade Wheel, MDPI, Basel, Switzerland, 2017.
13. Owusu-Ansah, P., et. al., Analysis of Permanent Magnets Bearings in Flywheel Rotor Designs, *Int. Journal of Engineering Research and Application*, Vol. 6, Issue 4, Part - 7, April, 2016, pp. 25-31.

14. Zingerli, C.M., Kolar, J.W., Novel observer based force control for active magnetic bearings, *Proceedings of the 2010 International Power Electronics Conference (IPEC)*, June 21-24, Sapporo, Japan, 2010, pp. 2189–2196.
15. Schneider, D.M., Control of processes with time delays, *IEEE Transactions on Industry Applications*, Vol. 24, No. 2, March/April, 1988, pp. 186-191.
16. Wurmsdobler, P., State Space Adaptive Control for a Rigid Rotor Suspended in Active Magnetic Bearings, Vienna University of Technology, Vienna, Austria, 1997.
17. ABB Group. Direct torque control. Technical guide No. 1, 2011.
18. Zhong, I., Rahman, M.F., et. al., Analysis of Direct Torque Control in Permanent Magnet Synchronous Motor Drives, *IEEE Transactions on Power Electronics*, Vol. 12, No. 3, May 1997, pp. 528-536.
19. Garcia, X. T., et. al., Comparison between FOC and DTC strategies for permanent magnet synchronous motors, *Advances in Electrical and Electronic Engineering*, Vol.5, March 2006.
20. Buja, G.S., Kazmierkowski, M.P., Direct torque control of PWM inverter-fed AC motors - a survey, *IEEE Transactions on Industrial Electronics*, vol. 51, no. 4, August 2004, pp. 744-757.
21. Wayne Bequette, B., Process Control. Modeling, Design and Simulation, Prentice Hall, Upper Saddle River, NJ, USA, 2003.
22. Franklin, G.F., Powell, J.D., Workman, M.L., Digital control of dynamic systems, 3rd edition, Addison Wesley Longman, Inc., USA, 1998.
23. Zhuravlyov, Y. N., On LQ-control of magnetic bearing, *IEEE Transactions on Control Systems Technology*, Vol. 8, No. 2, March 2000, pp. 344-350.
24. Schweitzer, G., Active magnetic bearings - chances and limitations, *IFToMM Sixth International Conference on Rotor Dynamics*, Sydney, Australia, 2002.